Cement and Concrete Research 144 (2021) 106404

Contents lists available at ScienceDirect

Cement and Concrete Research

journal homepage: www.elsevier.com/locate/cemconres

Hydro-chemo-mechanical phase field formulation for corrosion induced cracking in reinforced concrete

Congjie Wei [a], Charles S. Wojnar [b], Chenglin Wu [a,*]

[a] Department of Civil, Architectural, and Environmental Engineering, Missouri University of Science and Technology, Rolla, MO, USA
[b] Computational Engineering Division, Lawrence Livermore National Laboratory, Livermore, CA, USA

ARTICLE INFO

Keywords:
Corrosion
Diffusion
Fracture
Phase-field modeling

ABSTRACT

Steel corrosion induced cracking in reinforced concrete structures is often caused by volumetric straining at the steel-concrete interface. This volumetric strain is mainly controlled by the rate of generation of corrosion product, which depends on the diffusion of Cl^- and dissolved O_2 as well as the chemical reaction at the steel-concrete interface. While many numerical modeling techniques have been proposed to tackle this complex phenomenon, most have been limited to using staggered solution schemes, where the diffusion, chemical reaction, mechanical strain, and crack fields are solved for separately. Unfortunately, such approaches introduce numerical errors that can lead to unrealistic predictions. Therefore, a coupled solution, is needed to remove the formulation induced errors and understand this complex phenomenon.

To provide a unifying solution framework for corrosion induced cracking in reinforced concrete, a phase field formulation is presented and implemented with FEM algorithms. The governing equations are derived from the system's free energy and Fick's law of diffusion. The proposed formulation was first validated in 1D by comparing the modeling results with the semi-analytical solution approximated via Laurent series to avoid singularities in the complex domain. 2D plane strain solutions to the embedded rebar undergoing corrosion induced cracking with pre-cracks are also presented and compared with the approximated solutions from linear elastic fracture mechanics theory (LEFM). The modeling of crack propagation enabled by the proposed formulation is also presented along with parametric studies to reveal the roles of the fracture toughness and permeability of the concrete on the corrosion induced cracking. A case study was also conducted on H-pile steel with concrete jackets to demonstrate the feasibility of modeling corrosion induced fracture in reinforced concrete structures with complex steel-concrete interfaces.

1. Introduction

Corrosion is one of the most common reasons of serviceability deterioration of reinforced concrete structures [1–3]. For concrete structures exposed to aggressive environments, sea water or frozen soil for example, Cl^- tends to disrupt the original passive environment and cause the generation of rust products resulting in a larger volume compared to the original reinforcement volume, as illustrated in Fig. 1. This volume expansion leads to an outward radial pressure on the surrounding concrete. As a result, the inevitable micro-cracks introduced during concrete curing processes, as shown in Fig. 1a, will be under tension due to tensile hoop stress. This will lead to the damage and fracture of the concrete cover, as shown in Fig. 1c. Furthermore, these propagating cracks will create channels and accelerate the diffusive flow, which in turn increases the concentration of oxygen at the steel-concrete interface, and eventually accelerates the cracking of the surrounding concrete cover. A comprehensive numerical model for analyzing this diffusion-corrosion-fracture process will provide an effective tool to investigate the failure process of concrete covers with respect to crack initiation and propagation and provide further knowledge about the essential properties that influence the endurance and serviceability of reinforced concrete structures. Moreover, there have been few investigations of these effects within a framework that links the stress evolution and the crack propagation with the interfacial chemical reaction and the diffusivity change due to fracture evolution.

Previous models used to evaluate corrosion introduced fracture have mainly focused on fracture propagation. The volume expansion due to corrosion at the steel-concrete interface is introduced by applying an

* Corresponding author.
E-mail address: wuch@mst.edu (C. Wu).

https://doi.org/10.1016/j.cemconres.2021.106404
Received 28 May 2020; Received in revised form 27 December 2020; Accepted 22 February 2021
Available online 21 March 2021

artificial displacement boundary condition (i.e., Dirichlet boundary condition) [4]. This simplified volume expansion is approximated with semi-empirical models [5,6] or simplified physical or chemical processes. Pantazopoulou et al. [7] analyzed the crack induced stress softening in the cover concrete by driving forward the boundary condition based on rust production at a constant rate. El Maaddawy et al. [3] proposed a model for predicting the time duration from crack initiation to propagation. In their models, uniform internal radial pressure is assumed to be caused by the steel mass loss due to the corrosion process. Crack initiation within the concrete ring is considered to start when the hoop stress reaches the tensile strength of the concrete. Li et al. [8] derived an analytical model by assuming smeared cracks and obtained the critical crack propagation time. Most of these studies assumed a constant rate of corrosion and neglected the diffusion or the chemical reaction fields, which is essential to the corrosion process.

Recently, electrochemical corrosion models have been proposed [9,10]. With the presence of H_2O, O_2 and Cl^-, the Fe on the steel-concrete interface will be converted to its energetically stable form in nature, iron oxides and iron hydroxides. The accumulated rust could be a mixture of Fe_2O_3, Fe_3O_4, $Fe(OH)_2$, and $Fe(OH)_3$ among many other possible products, depending on the environment, reinforcement and concrete type. As shown in Fig. 2, at the active sites of the reinforcement, where the steel-concrete interface is exposed to the aggressive solutions with O_2 and Cl^-, a so-called anode is formed. The anodic reaction transforms Fe into free ferrous irons and electrons or iron oxides,

$$Fe \rightarrow Fe^{2+} + 2e^-, \tag{1}$$

$$2Fe + 3H_2O \rightarrow Fe_2O_3 + 6H^+ + 6e^-. \tag{2}$$

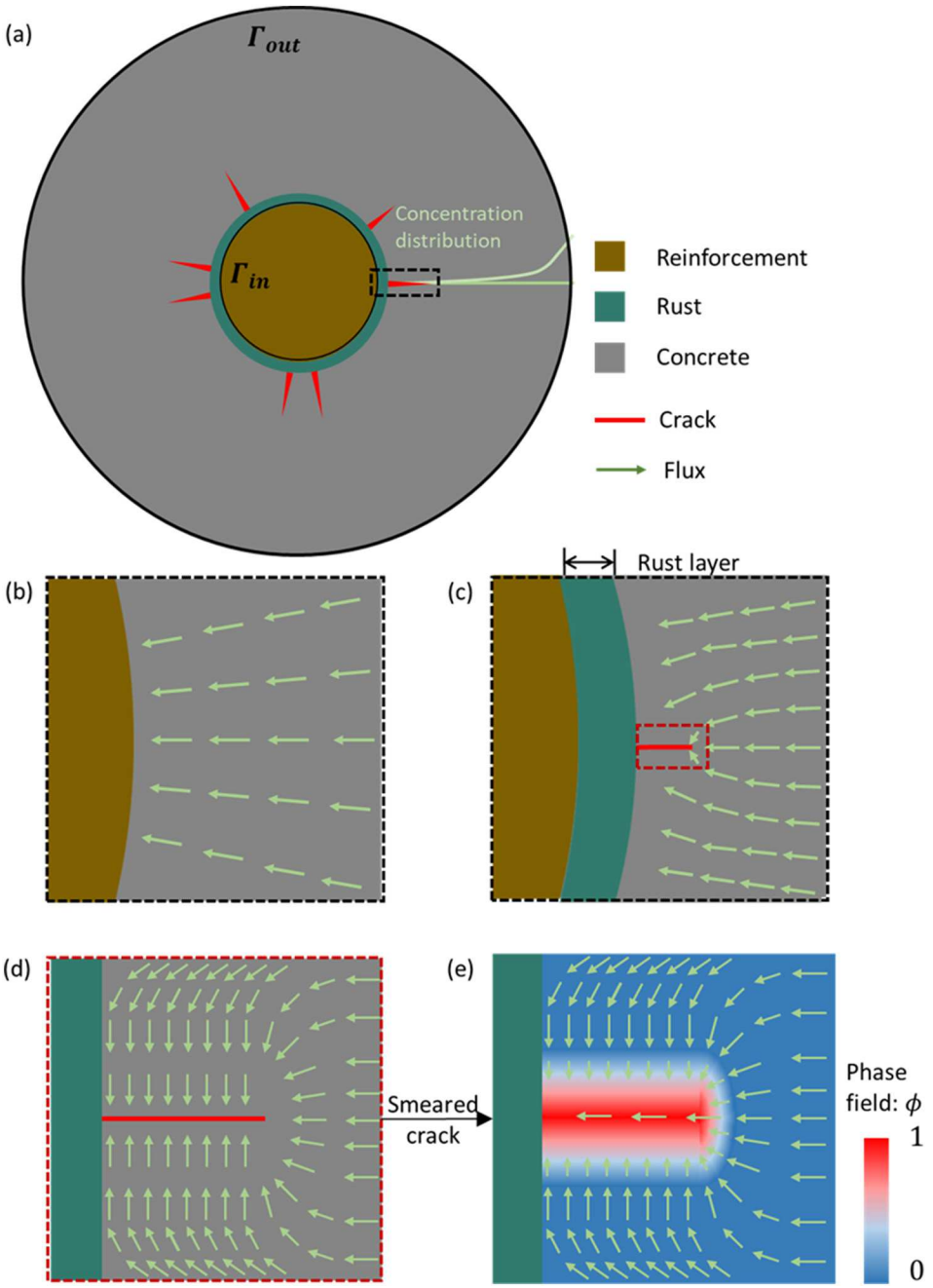

Fig. 1. (a) Corrosion of reinforcement-concrete interface. (b) Dissolved O_2, Cl^- diffusion flux in intact concrete. (c) Rust development and crack influence on diffusion flux. (d) Local diffusion flux around crack. (e) Crack smeared with phase field.

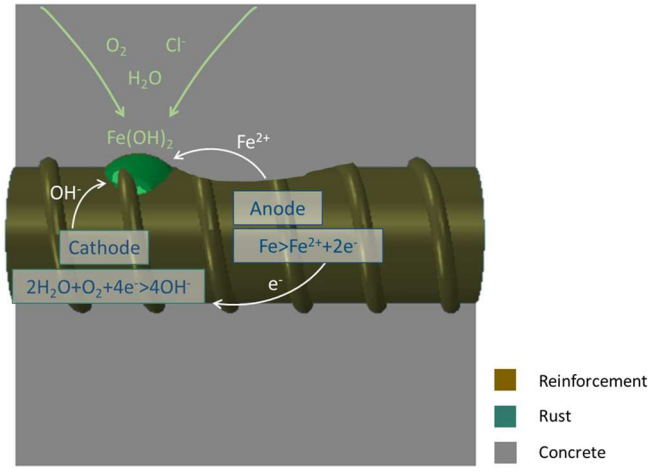

Fig. 2. Corrosion process in reinforced concrete.

The remaining part of the reinforcement forms the cathode where the free electrons combine with H_2O and O_2 and form the hydroxides,

$$2H_2O + O_2 + 4e^- \rightarrow 4OH^-. \quad (3)$$

On the steel-concrete interface, the Fe^{2+} ions and OH^- ions react to maintain overall electrical neutrality and form iron hydroxide, which is also called the rust,

$$Fe^{2+} + 2OH^- \rightarrow Fe(OH)_2. \quad (4)$$

This initially generated iron hydroxide may be oxidized further by dissolved oxygen,

$$4Fe(OH)_2 + 2H_2O + O_2 \rightarrow 4Fe(OH)_3. \quad (5)$$

This continuously generated rust leads to the radial pressure on the concrete cover until a crack initiates and propagates to the surface. Knowing that the final rust production and composition depends on the availability of dissolved O_2 and surface pH value, many studies have investigated the volumetric change in this process, which plays an important role in fracture analysis of the concrete cover. Yu et al. [11] proposed a macro-cell corrosion model and predicted the corrosion rate of steel reinforcement in concrete structures based on the electrochemical principles. Cao et al. [12] conducted electrochemical analysis on the coupled micro- and macro-cell corrosion process where oxygen concentration and electrical potential distribution within the concrete cover were considered. The crack width evolution was then modeled based on a uniform thick-walled cylinder model. Nossoni et al. [13] developed an electrochemical-mechanistic model where the accumulation of rust was related to the concentration of dissolved O_2 on the interface. This volume expansion led to the internal radial pressure, which in turn drove the rust products to diffuse into the concrete pores. These models effectively simulated the steel-concrete interfacial corrosion process linked to a known diffusion field. However, the crack evolution is mostly neglected. The diffusivity change due to the fracture evolution was also not considered. Moreover, these electrochemical models are often computationally costly and may raise numerical issues if coupled with mechanical and fracture fields.

To combine mechanical and fracture fields into the multi-physics problem, a phase field approach is proposed. Due to the discrete nature of cracks, the classical finite element methods (FEM) is not equipped to predict crack propagation, branching, and merging behaviors. There are several approaches to solve these problems such as extended finite element methods [14,15], meshless methods [16], and boundary element methods [17,18]. However, most of these approaches require re-meshing algorithms or a pre-defined crack propagation path, which greatly limited their application to problems with complex fracture patterns.

Rashid pioneered the concept of a smeared crack model for the simulation of concrete applications [19]. By smearing the crack into a scalar phase field parameter, ϕ, where $\phi = 0$ represents intact material and $\phi = 1.0$ represents fully damaged material, the phase field method turns the problem into a continuous one. Later on, Francfort and Marigo proposed a variational free-discontinuity formulation for brittle fracture [20]. Msekh et al. [21] and Liu et al. [22] implemented phase field algorithms for brittle fracture within the commercial software Abaqus. Ambati et al. [23] and Borden et al. [24] extended the algorithms to model ductile fracture problems. Benefiting from the continuous scheme of the phase field method, it is suitable for coupling with thermal, electrical, chemical or other fields [25,26]. Moreover, corrosion and diffusion problems have been modeled using the phase field method; Emilio et al. [27] coupled the phase field model with hydrogen diffusion where the fracture energy degradation due to the presence of hydrogen was modeled in metallic materials. Mai [28,29] modeled galvanic and pitting corrosion by relating the anodic current density to the interface kinetics parameter. For cementitious materials, Nguyen et al. [25] investigated shrinkage fracture in early-age cement using the phase field method. Wu et al. [30] coupled the diffusion field with the phase field parameter in hardened cement material by setting the diffusive coefficient dependent on the phase field gradient. The dissolved O_2 flux along the crack propagation direction was compared to analytical solutions, which verified the diffusivity enhancement along the crack. However, the flux change along the direction perpendicular to the crack was not considered, which may play an important role within fracture problems under complex boundary conditions. The boundary conditions in their study are also applied artificially rather than linked to rust accumulation. Until now, a comprehensive model with fully interacted diffusion, corrosion, mechanical and fracture fields for reinforced concrete structures has not been developed.

The rest of the paper is structured as follows. In Section 2, the formulation of a phase field model fully interacted with diffusion, corrosion, and mechanical fields is presented via an energetic perspective, from which the governing equations are derived. This model is then implemented using finite element analysis algorithms within Abaqus. In Section 3, analytical solutions for the 1D concentration distribution are derived and singular points for fully fractured scenarios are approximated via Laurent series expansion with controllable error. A 1D finite element model is constructed and verified with analytical results. In Section 4, the corrosion-fracture coupling is conducted by relating the volume expansion to a stable diffusion field with constant diffusive coefficient. In addition, a plane strain finite element model is constructed and compared with analytical results obtained with linear elastic fracture mechanics (LEFM). In Section 5, a phase field model for the mechanical strain and fracture fields is coupled with diffusion fields and corrosion processes. This model is applied on quarter circular and H-pile steel with concrete jacket cases. Parameter studies are conducted to determine the influence of material properties on the endurance of the concrete cover. Section 6 closes the paper with conclusions and discussions.

2. Formulation

In this paper, we aim to construct a multi-physics FEM model where diffusion, corrosion, mechanical and fracture fields are fully interacted to study the failure of the concrete cover due to corrosion. The diffusion field is (1) coupled with the phase field parameter to model the diffusivity change due to material property degradation, (2) the corrosion process is coupled with the diffusion field by relating the rust expansion rate to the amount of dissolved O_2 diffused to the steel-corrosion interface, and (3) the mechanical-fracture field in concrete cover is coupled with this volume change. In our analysis, homogeneous mechanical and diffusive properties are considered for the concrete cover.

2.1. Coupling of diffusion-corrosion-mechanics-fracture fields

As shown in Fig. 3, the multi-physics model presented in our paper has the following main components.

i. *Corrosion process influenced by diffusion field change*

Under saturated or high relative humidity environments, the diffusion coefficient of the oxygen within concrete will be the controlling factor of the anodic and cathodic reactions [31–33]. The low amount of dissolved O_2 arriving at the interface between the reinforcement and concrete limits the rate of rust generation. Based on the corrosion process described in Section 1, the corrosion rate is related to the dissolved O_2 flux at the steel-concrete interface. The generation of rust, where iron hydroxides is assumed to compose the main part of the rust, is modeled based on the cathodic limiting reaction. The rust thickness development, δ, is estimated in [13] with

$$\frac{d\delta}{dt} = \frac{C_2\left(j_{Fe(OH)_2} - j_{Fe(OH)_3}\right)A_{Fe(OH)_2}}{\rho_{Fe}} + \frac{C_3 j_{Fe(OH)_3} A_{Fe(OH)_3}}{\rho_{Fe}}, \tag{6}$$

where $j_{Fe(OH)2}$ and $j_{Fe(OH)3}$ are fluxes related to the limiting dissolved O_2 flux on the steel-concrete interface, $A_{Fe(OH)2}$ and $A_{Fe(OH)3}$are contacting areas, ρ_{Fe} is the iron density, and C_2 and C_3 are constants. Considering all electrochemical processes and their coupling with mechanical and fracture fields is unrealistic and computational inefficient. To make the problem more amenable to numerical implementation while maintaining the physics of the corrosion rate relation to the dissolved O_2 flux, a simplified model relating the volume expansion rate of the rust layer directly to the dissolved O_2 flux is introduced. It is assumed here that all of the dissolved O_2 flux is consumed in the corrosion process, considering that the diffusion process in the concrete is relatively slow compared to the production of the rust. A linear correlation is assumed:

$$\frac{\Delta v}{V} = \alpha \int_{\partial\Omega} \boldsymbol{j}\cdot\boldsymbol{n} dA = -\alpha D \int_{\partial\Omega} t\nabla C\cdot\boldsymbol{n} dA, \tag{7}$$

where C is the concentration of dissolved O_2 and V and Δv are the original volume and change in volume, respectively, of the steel-concrete interface layer where the corrosion process happens, referred to as the rust layer as shown in Fig. 1a. D is the diffusion coefficient. This rust layer in reinforced concrete structures normally ranges between 40 and 100 μm[34–36], we choose the median, i.e., 70 μm as the rust layer thickness in our modeling. Also, $\boldsymbol{j}$ is the dissolved O_2 flux related to the gradient of concentration field with $\boldsymbol{j} = -D\nabla C$. Furthermore, $\boldsymbol{n}$ is the surface normal, α is the volume expansion per mole of dissolved O_2, $\partial\Omega$ is the contacting area between rust layer and concrete, and t is time. The corrosion rate versus unit dissolved O_2 flux for a changing environment could be adjusted with α based on the main rust production type. Quadratic or other types of relations could also be adopted depending on the specific corrosion processes.

It is assumed that the reinforcement surrounded by the rust layer is not corroded and thus has no volume change, the interface between reinforcement and rust layer is fixed with respect to displacement d.o.f.s in the numerical modeling. Meanwhile, the interface between rust layer and concrete cover is free to move.

ii. *Stress field influenced by corrosion process*

The volume expansion of the rust layer creates an increasing radial pressure on the concrete cover, resulting in tensile hoop stresses and

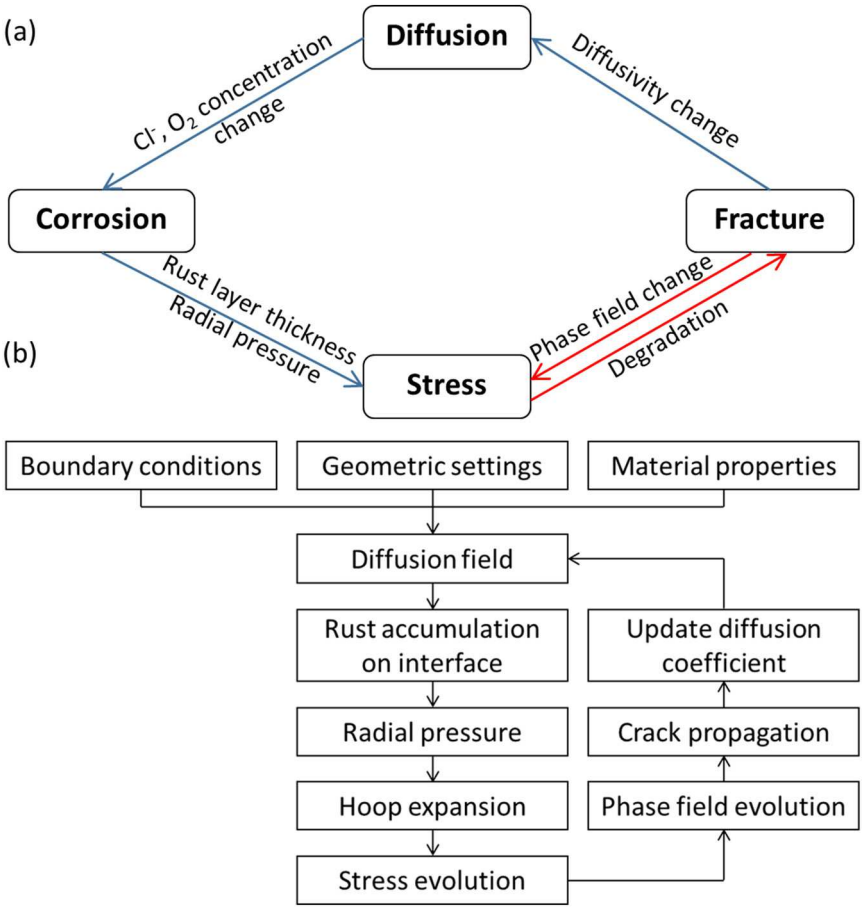

Fig. 3. (a) Coupling of diffusion-fracture-corrosion fields. (b) Calculation flow chart for the FEM implementation.

quasi-mode-I fracture scenarios for micro-cracks as shown in Fig. 1a.

iii. *Mechanical-fracture field evolution*

The phase field fracture parameter increases with increasing tensile stress. Once the critical energy release rate is reached, the crack starts to propagate until reaching the surface of the concrete cover, and in turn degrades the material properties. This is captured via the phase field parameter, ϕ, which increases in the direction of the propagating crack.

iv. *Diffusivity change due to material degradation*

Newly generated cracks create channels and accelerate the diffusion, which has been observed in experiments [37,38]. These channels create connected paths for dissolved O_2 diffusion and thus the diffusivity is vastly enhanced along the crack. Meanwhile, the diffusivity remains the same along the direction normal to the crack. This coupling is modeled by setting the diffusion coefficient as a second order tensor, $\boldsymbol{D}$, and relating it to the phase field parameter, ϕ, which was given in [30] by

$$\boldsymbol{D}(\phi) = D(1-\phi^m)\boldsymbol{I} + \phi^m D(\boldsymbol{I} - \boldsymbol{n_1}\otimes\boldsymbol{n_1}), \tag{8}$$

where D is the diffusivity for intact concrete, m is an adjustable power parameter, $\boldsymbol{I}$ is the identity matrix, $\boldsymbol{n_1} = \frac{\nabla\phi}{||\nabla\phi||}$ is the unit vector orthogonal to the crack plane. Since the diffusivity has little direct influence on the toughness of concrete materials, the diffusivity is one-way coupled to the phase field, while the phase field evolution is not directly linked to the diffusion field.

2.2. Governing equations

The governing equations in this paper are generated using the Rayleigh-Ritz method via an energetic approach [39] as well as Fick's law of diffusion. The potential energy, Π, of the concrete occupying a region Ω is assumed to be composed of 3 parts: the elastic energy ψ_{el} with independent variables of total strain $\boldsymbol{\varepsilon}$ and degraded by phase field parameter ϕ, the fracture energy ψ_{frac} with a single independent variable, the phase field ϕ (these 2 parts compose the total stored energy density ψ), and external work W as shown in following equation:

$$\Pi = \int_\Omega \psi dV - W = \int_\Omega (\psi_{el} + \psi_{frac}) dV - W, \tag{9}$$

where $\psi_{el} = \left((1-\phi)^2 + k\right)\Phi(\boldsymbol{\varepsilon}) = \frac{1}{2}\left((1-\phi)^2 + k\right)\boldsymbol{\varepsilon}\cdot\boldsymbol{E}\boldsymbol{\varepsilon}$ with $\boldsymbol{E}$ being the elastic modulus tensor, $\boldsymbol{\varepsilon} = \text{sym}\,(\nabla\boldsymbol{u})$ is the total strain related to the displacement field $\boldsymbol{u}$, $\Phi(\boldsymbol{\varepsilon}) = \boldsymbol{\varepsilon}\cdot\boldsymbol{E}\boldsymbol{\varepsilon}$ is the elastic energy of the undamaged material. Linearized kinematics is assumed here in order to adopt the small-strain tensor concepts. A quadratic degradation function ($(1-\phi)^2 + k$) is assumed, where k is a parameter keeping the system well-conditioned during the simulation. The constitutive equation for stress can be expressed as $\boldsymbol{\sigma} = \frac{\partial\psi}{\partial\boldsymbol{\varepsilon}}$. It should be noted that the diffusion has no direct influence on the stress and phase field for concrete, thus the total strain is equal to the elastic strain. For rust layer elements, the elastic strain $\boldsymbol{\varepsilon_{el}}$ is related to total strain, $\boldsymbol{\varepsilon}$, and strain caused by corrosion, $\boldsymbol{\varepsilon_c}$, with $\boldsymbol{\varepsilon_{el}} = \boldsymbol{\varepsilon} - \boldsymbol{\varepsilon_c}$. Then the elastic energy function would change to $\Phi(\boldsymbol{\varepsilon}) \rightarrow \Phi(\boldsymbol{\varepsilon_{el}})$. For equilibrium expansion along all directions (in 2D), $\boldsymbol{\varepsilon_c}$ is obtained with

$$\boldsymbol{\varepsilon_c} = -\frac{1}{2}\left(\alpha D\int_{\partial\Omega} t\nabla C\cdot\boldsymbol{n}dA\right)\boldsymbol{I}. \tag{10}$$

The symbols have the same definitions as those in Eq. (7). The fracture energy part is given by

$$\psi_{frac}(\phi,\nabla\phi) = \frac{G_c}{2}\left(\frac{1}{\ell_0}\phi^2 + \ell_0\nabla\phi\cdot\nabla\phi\right), \tag{11}$$

where G_c is the critical energy release rate and ℓ_0 is the regularization scale parameter. The external work is given by

$$W = \int_\Omega \boldsymbol{b}\cdot\boldsymbol{u}dV + \int_{\partial\Omega_t}\boldsymbol{h}\cdot\boldsymbol{u}dA, \tag{12}$$

where $\boldsymbol{b}$ and $\boldsymbol{h}$ are the body force and the traction on surface $\partial\Omega_t$, respectively.

The governing equations regarding the displacement and phase field correspond to the Euler-Lagrange equation of the potential energy, which are found by taking the first variation of the potential energy with respect to each field variable, the derivation details could be found in our previous paper about phase field [40] and the resulting Gateaux derivatives are shown as follows,

$$D_{\delta u}\Pi = -\int_\Omega(\nabla\cdot\boldsymbol{\sigma} + \boldsymbol{b})\cdot\delta\boldsymbol{u}dV + \int_{\partial\Omega_t}(\boldsymbol{\sigma n} - \boldsymbol{h})\cdot\delta\boldsymbol{u}dA, \tag{13a}$$

$$D_{\delta\phi}\Pi = \int_\Omega\left(\frac{\partial\psi_{el}}{\partial\phi} + \frac{G_c\phi}{\ell_0} - G_c\ell_0\nabla^2\phi\right)\delta\phi dV + \int_{\partial\Omega} G_c\ell_0\nabla\phi\cdot\boldsymbol{n}\delta\phi dA. \tag{13b}$$

Considering that potential energy formulations for diffusion process is too simplified and may loss authenticity within our formulation, we instead used the well verified Fick's law of diffusion to construct the model. For a diffusion process following Fick's law, the concentration field is governed by

$$\dot{C} = \nabla\cdot(\boldsymbol{D}\nabla C), \tag{14}$$

where the diffusion coefficient, $\boldsymbol{D}$, is dependent on phase field parameter via Eq. (8). For the sake of simplification without considering the secondary derivatives, we neglect the spatial derivative of phase field in the $\boldsymbol{D}$ term; Eq. (14) is approximated with

$$\dot{C} = (D(1-\phi^m)\boldsymbol{I} + \phi^m D(\boldsymbol{I} - \boldsymbol{n_1}\otimes\boldsymbol{n_1}))\nabla^2 C. \tag{15}$$

To verify that this approximation has only limited error, in Section 3, we derived the analytical solutions of Eq. (14) and obtained the numerical solution of its approximation, Eq. (15), based on 1-D scenario, the results fit well with each other.

Based on Eqs. (13a), (13b)–(15), the governing equations are obtained as

$$\nabla\cdot\boldsymbol{\sigma} + \boldsymbol{b} = 0 \text{ in } \Omega, \tag{16a}$$

$$\dot{C} = (D(1-\phi^m)\boldsymbol{I} + \phi^m D(\boldsymbol{I} - \boldsymbol{n_1}\otimes\boldsymbol{n_1}))\nabla^2 C \text{ in } \Omega, \tag{16b}$$

$$-2(1-\phi)\Phi(\boldsymbol{\varepsilon}) - G_c\ell_0\nabla^2\phi + G_c\frac{1}{\ell_0}\phi = 0 \text{ in } \Omega, \tag{16c}$$

$$\boldsymbol{u} = \overline{\boldsymbol{u}} \text{ on } \partial\Omega\backslash\partial\Omega_t,\ C = \overline{C} \text{ on } \partial\Omega, \tag{16d}$$

$$\boldsymbol{\sigma n} = \boldsymbol{h} \text{ on } \partial\Omega_t. \tag{16e}$$

In these equations, Eq. (16a) is the balance of linear momentum, Eq. (16b) is Fick's law and defines the coupling between diffusion and the phase field parameter, Eq. (16c) controls the phase field evolution and Eq. (16d)-(16e) are boundary conditions. The applied displacement is $\overline{\boldsymbol{u}}$ and the applied concentration is $\overline{C}$. In this model, the phase field evolution is constrained to be within the concrete material by setting the critical energy release rate of reinforcement and rust layer to a large number to avoid damage development. In the following sections, the coupling between diffusion-fracture fields and corrosion-fracture fields are separately constructed and verified with analytical solutions. It should be noted that this formulation assumes monotonic loading scenarios, where no unloading or crack closure are considered.

2.3. Finite element method implementation

Based on the formulation and governing equations, a finite element

model is constructed with a flow chart as shown in Fig. 3b. The process follows typical FEM procedures that could be found in references such as [39,41] and implemented within Abaqus. UEL and UMAT subroutine files are coded to include the user defined element and material behavior. 3-Node triangle elements with plane strain conditions are considered as example in this paper.

With the domain being divided with 3-node triangle elements, shape functions are first used for interpolation of displacement, phase field parameter, and concentration inside each element via

$$\begin{pmatrix} u_x \\ u_y \end{pmatrix} = \boldsymbol{N_u u^e}, \tag{17a}$$

$$\phi = \boldsymbol{N_\phi \phi^e}, \tag{17b}$$

$$C = \boldsymbol{N_C C^e}, \tag{17c}$$

where $\boldsymbol{\phi^e}$, $\boldsymbol{C^e}$, and $\boldsymbol{u^e}$store node values for the phase field, concentration, and the displacement components for each element, respectively. The shape function vectors/matrices, $\boldsymbol{N_u}$, $\boldsymbol{N_\phi}$ and $\boldsymbol{N_C}$ are constructed with shape functions, N_1, N_2 and N_3, and are defined as

$$\boldsymbol{N_u} = \begin{bmatrix} N_1 & 0 & N_2 & 0 & N_2 & 0 \\ 0 & N_1 & 0 & N_2 & 0 & N_2 \end{bmatrix}, \tag{18a}$$

$$\boldsymbol{N_\phi} = \boldsymbol{N_C} = [N_1 \quad N_2 \quad N_3] \tag{18b}$$

The strain, phase field and concentration field gradients are obtained with B-matrices, $\boldsymbol{B_u}$, $\boldsymbol{B_{\nabla\phi}}$ and $\boldsymbol{B_{\nabla C}}$, which are composed with derivatives of shape functions,

$$\boldsymbol{\varepsilon} = \boldsymbol{B_u u^e}, \tag{19a}$$

$$\nabla\phi = \boldsymbol{B_{\nabla\phi}}\phi^e, \tag{19b}$$

$$\nabla C = \boldsymbol{B_{\nabla C} C^e}. \tag{19c}$$

The displacement and phase field parameter in the concrete are solved using a two-step approach: First, we provide an initial condition for the oxygen concentration in the concrete (usually zero) to determine the strain of the rust layer, then we solve for the resulting equilibrium state for the displacement and fracture minimizing the potential energy by solving the following equation,

$$\begin{bmatrix} \boldsymbol{K^u} & \boldsymbol{K^{u\phi}} \\ \boldsymbol{K^{\phi u}} & \boldsymbol{K^\phi} \end{bmatrix} \begin{bmatrix} \boldsymbol{u} \\ \boldsymbol{\phi} \end{bmatrix} = \begin{bmatrix} \boldsymbol{r^u} \\ \boldsymbol{r^\phi} \end{bmatrix} \tag{20}$$

By replacing the displacement and phase field in Eq. (16a), c with the nodal values and B-matrices and taking first derivatives, the right hand side (RHS) terms, $\boldsymbol{r^u}$ and $\boldsymbol{r^\phi}$ in Eq. (20), are obtained by assembling their local (element) contributions denoted by the additional superscript e,

$$\boldsymbol{r^{u,e}} = \int_{\Omega_e} \left[(1-\phi)^2 + k\right] \mathbf{B}_u^T \boldsymbol{E B_u u^e} d\mathrm{V}, \tag{21a}$$

$$\boldsymbol{r^{\phi,e}} = \int_{\Omega_e} \left(G_c \ell_0 \boldsymbol{B_{\nabla\phi}^T B_{\nabla\phi} \phi^e} + \left[\frac{G_c}{\ell_0} + (\boldsymbol{u^e})^T \boldsymbol{B_u^T E B_u u^e}\right] \boldsymbol{N_\phi^T N_\phi \phi^e} - \left((\boldsymbol{u^e})^T \boldsymbol{B_u^T E B_u u^e}\right) \boldsymbol{N_\phi^T} \right) dV, \tag{21b}$$

where Ω_e is the volume of an element, $\boldsymbol{E}$ is the elastic modulus matrix (assumed to be written following Voigt notation).

The element stiffness matrices, $\boldsymbol{K^{uu,e}}$, $\boldsymbol{K^{u\phi,e}}$, $\boldsymbol{K^{\phi u,e}}$ and $\boldsymbol{K^{\phi\phi,e}}$ (assembled to get the global terms in Eq. (20)), are obtained by differentiating the RHS terms with respect to incremental nodal values of displacement and phase field,

$$\boldsymbol{K^{uu,e}} = \frac{\partial \boldsymbol{r^{u,e}}}{\partial \boldsymbol{u^e}} = \int_{\Omega_e} \left((1-\phi)^2 + k\right) \boldsymbol{B_u^T E B_u} dV, \tag{22a}$$

$$\boldsymbol{K^{u\phi,e}} = \frac{\partial \boldsymbol{r^{u,e}}}{\partial \boldsymbol{\phi^e}} = \int_{\Omega_e} -2(1-\phi) \boldsymbol{B_u^T (E\varepsilon) N_\phi} dV, \tag{22b}$$

$$\boldsymbol{K^{\phi u,e}} = \frac{\partial \boldsymbol{r^{\phi,e}}}{\partial \boldsymbol{u^e}} = \int_{\Omega_e} -2(1-\phi) \boldsymbol{N_\phi^T (E\varepsilon)^T B_u} dV, \tag{22c}$$

$$\boldsymbol{K^{\phi\phi,e}} = \frac{\partial \boldsymbol{r^{\phi,e}}}{\partial \boldsymbol{\phi^e}} = \int_{\Omega_e} \left(G_c \ell_0 \boldsymbol{B_{\nabla\phi}^T B_{\nabla\phi}} + \left(\frac{G_c}{\ell_0} + (\boldsymbol{u^e})^T \boldsymbol{B_u^T E B_u u^e}\right) \boldsymbol{N_\phi N_\phi^T} \right) dV. \tag{22d}$$

To solve for the evolution of the concentration distribution over time, we enforce Fick's law in Eq. (14). In order to solve the PDE in the context of FEM, we convert it to the weak form using the Galerkin-weighted-residual method. From there we substitute our FEM interpolation scheme and obtain the semi-discrete equation for Fick's law:

$$\boldsymbol{M_c}\, \dot{\boldsymbol{C}} + \boldsymbol{K_c C} = \boldsymbol{0}, \tag{23}$$

where $\boldsymbol{M_c}$ is the viscosity matrix, $\boldsymbol{K_c}$ is the stiffness matrix, and $\boldsymbol{C}$ is a vector containing the nodal values of the concentration. The subscript "c" is to distinguish from the corresponding terms for the elastic and fracture part of the simulation. The element viscosity matrix and element stiffness matrix are

$$\boldsymbol{M_c^e} = \int_{\Omega_e} N^T N dV, \; \boldsymbol{K_c^e} = \int_{\Omega_e} \boldsymbol{B_{\nabla C}^T D B_{\nabla C}} dV, \tag{24}$$

which are then assembled to obtain their global counterparts. Finally, to solve for the concentration evolution over time, we apply the forward Euler method to the semi-discrete equation (Eq. (23)),

$$\boldsymbol{C^{n+1}} = \boldsymbol{C^n} - \Delta t \boldsymbol{M_c^{-1} K_c C^n}, \tag{25}$$

where the superscripts n and $n+1$ denote the timestep and Δt is the timestep size.

With the concentration distribution updated via Eq. (25), the rate of dissolved O_2 involved in the corrosion process is obtained as

$$\dot{O}_2 = \int_{\partial\Omega} \boldsymbol{j}\cdot\boldsymbol{n} dA = -\int_{\partial\Omega} (\boldsymbol{D}\nabla C)\cdot\boldsymbol{n} dA. \tag{26}$$

The corrosion introduced strain change of rust layer is then updated in accordance with this diffusion field change and further influences the displacement and phase field change in the concrete domain of the next step.

For each modeling case, the geometry, material properties, modeling steps and boundary condition settings are included in a corresponding Abaqus input file. To define initial conditions and run a time dependent analysis for the concentration field, the modeling steps should be set as mechanical-temperature coupling steps where the concentration occupies the degree of freedom of the temperature field. In this manner, the density and specific heat variables are necessary for the calculation to move on but has no use for our analysis, thus these two variables are set as 1.0. The meshing should be refined and the element size for the expected crack propagation area should be lower than $0.1\ell_0$ for accuracy consideration. In our plane strain models, 3-node triangular elements with 1 Gauss integration point were used, making use of its adaptability for complex geometries. Due to the limitations in Abaqus, the visualization was achieved by supplementary dummy elements composed with standard Abaqus elements and the user defined element nodal values are assigned to these dummy elements.

3. Diffusion-fracture coupling verification

To verify the coupling between the diffusion field and the phase field, the analytical solutions for a 1D problem are derived. A singularity point is found when the phase field reaches 1.0, corresponding to a fully cracked scenario. A Laurent series is used to approximate the solution to this singularity point with controllable error. Derivation details could be

found in Section A of the Appendix. A finite element model is then constructed and compared with the analytical solution.

3.1. Analytical solution

For the diffusion-fracture coupling governing equation in Eq. (16b) under plain strain conditions, and for a static diffusion state $\frac{dC}{dt} = 0$, the normal direction of the phase field parameter is

$$\boldsymbol{n_1} = \frac{\nabla\phi}{||\nabla\phi||} = \frac{1}{||\nabla\phi||}\begin{bmatrix}\frac{\partial\phi}{\partial x}\\ \frac{\partial\phi}{\partial y}\end{bmatrix}, \tag{27}$$

where $||\nabla\phi|| = \left(\left(\frac{\partial\phi}{\partial x}\right)^2 + \left(\frac{\partial\phi}{\partial y}\right)^2\right)^{\frac{1}{2}}$.

For a plate with geometry shown in Fig. 4a, it is fixed at the boundary where $x = 0$ and stretched homogeneously along the positive x-direction at the right end boundary $x = 1.0$. This plate is set to have uniform Young's modulus and critical energy release rate other than the compliant middle spot, which has a much lower critical energy release rate comparing with other locations. This centered crack could be smeared by a phase field distribution with following equation, as demonstrated in [42],

$$\phi(x) = \phi_0 exp\left(-\frac{|x-a|}{\ell_0}\right), \tag{28}$$

where $a = \frac{1}{2}$ is the compliant spot location and ϕ_0 is the phase field value at $x = a$.

In 1D, the variation of the phase field along the y-direction can be neglected or set $\frac{\partial\phi}{\partial y} = 0$. Eq. (27) then becomes

$$\boldsymbol{n_1} = \begin{bmatrix}1\\0\end{bmatrix} \tag{29}$$

The diffusion coefficient tensor is then

$$\boldsymbol{D} = (D(1-\phi^m)\boldsymbol{I} + \phi^m D\,(\boldsymbol{I} - \boldsymbol{n_1}\otimes\boldsymbol{n_1})) = \begin{bmatrix}D(1-\phi^m) & 0\\ 0 & D\end{bmatrix} \tag{30}$$

Plugging Eq. (30) into Eq. (14) yields

$$\nabla\cdot((D(1-\phi^m)\boldsymbol{I} + \phi^m D\,(\boldsymbol{I} - \boldsymbol{n_1}\otimes\boldsymbol{n_1}))\nabla C) = -mD\phi^{m-1}\frac{\partial\phi}{\partial x}\frac{\partial C}{\partial x} + D(1-\phi^m)\frac{\partial^2 C}{\partial x^2} = 0. \tag{31}$$

Rearranging, Eq. (31) becomes,

$$m\phi^{m-1}\frac{\partial\phi}{\partial x}\frac{\partial C}{\partial x} = (1-\phi^m)\frac{\partial^2 C}{\partial x^2}. \tag{32}$$

For a phase field distribution described in Eq. (28), for $x < a$,

$$\frac{\partial^2 C}{\partial x^2} - \frac{\phi_0^m m exp\left(\frac{m(x-a)}{\ell_0}\right)}{\ell_0\left(1-\phi_0^m exp\left(\frac{m(x-a)}{\ell_0}\right)\right)}\frac{\partial C}{\partial x} = 0. \tag{33}$$

The general solution for this ordinary differential equation is

$$C = \frac{C_2\ell_0}{D}\left(-\frac{(x-a)}{\ell_0} + \frac{1}{m}ln\left(\phi_0^{-m} - exp\left(\frac{m(x-a)}{\ell_0}\right)\right)\right) + C_3. \tag{34}$$

Following a similar process, the general solutions for $x > a$ is

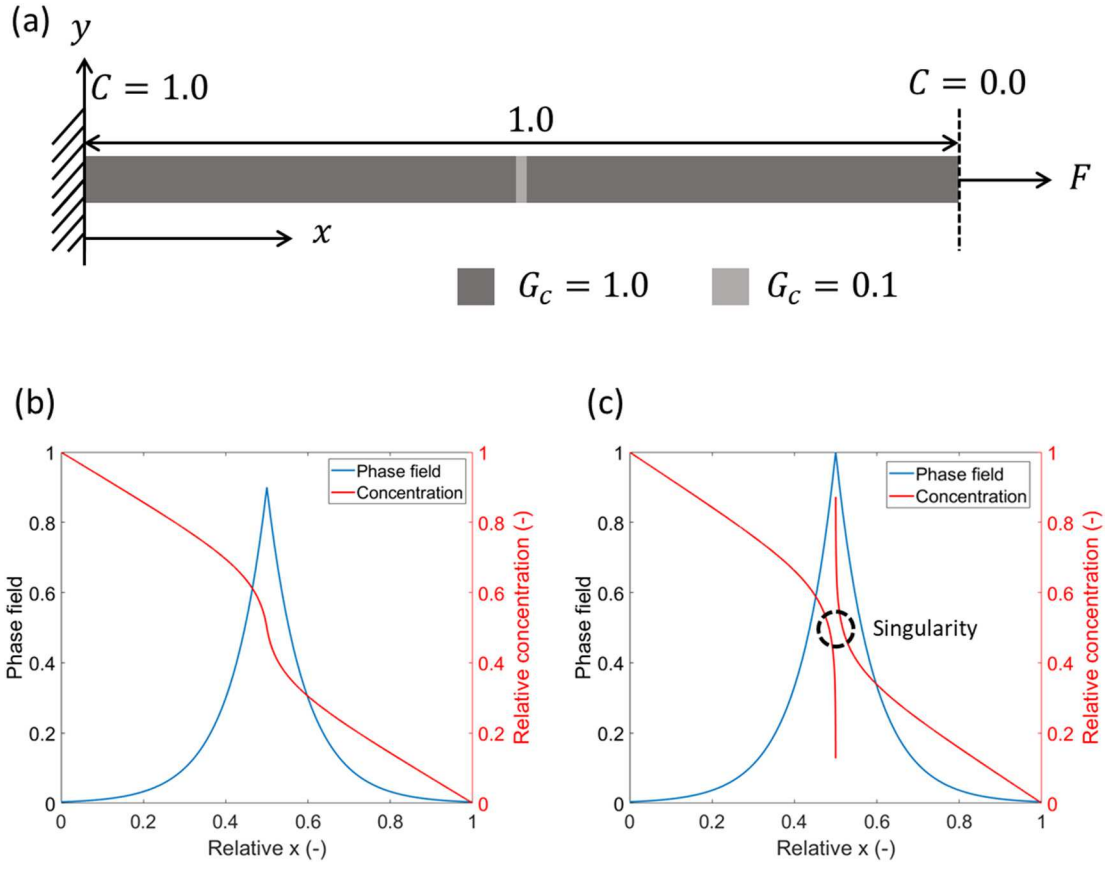

Fig. 4. (a) Geometric and parameter setup. Phase field and concentration distribution for (b) $\phi_0 = 0.9$ and (c) $\phi_0 = 1.0$. Geometric variables are normalized by the domain length as shown in (a), concentration values are normalized by the left end concentration.

$$C = \frac{C_4 \ell_0}{D}\left(-\frac{(x-a)}{\ell_0} - \frac{1}{m} ln\left(\phi_0^{-m} - exp\left(-\frac{m(x-a)}{\ell_0}\right)\right)\right) + C_5, \quad (35)$$

where C_2through C_5 are constants depending on the concentration boundary conditions. The detailed derivation can be found in the Sections A.1–A.2 of Appendix A. For the concentration boundary conditions shown in Fig. 4a, two solutions are calculated for $\phi_0 = 0.9$ and $\phi_0 = 1.0$ and are shown in Fig. 4b-c. A singularity point is found when $\phi_0 = 1.0$. The concentration tends to $+\infty$ as x tends to a^-, and tends to $-\infty$ as x tends to a^+. From a numerical perspective, this is due to the singularity point of the logarithm terms in Eqs. (34) and (35). This corresponds to a physical scenario where the plate is totally broken where $x = \alpha$, thus the diffusion process is completely blocked along the x-direction. However, a closed-form solution cannot be found to describe this singular behavior in this extreme situation. Approximation solutions are then sought which is described in the following section.

3.2. Approximation of singularity with Laurent series

For a better understanding of the diffusion-fracture coupling around a singularity Laurent series expansion is adopted to obtain an approximation with controllable error. The detailed derivation is shown in Section A.3 of the Appendix, where the Eq. (33) is reformed and expanded with Laurent series for integration with finite terms.

The Laurent series is a generalized version of the Taylor series and composed with positive and/or negative power components. Being expanded in the complex plane, one major advantage of Laurent series over Taylor series is the capability to approximate around singular points for analytic functions.

For $x < a$, take $j = -D\frac{dC}{dx}$ as the flux, where D is the diffusion coefficient, take $L = \frac{(x-a)}{\ell_0}$ for simplicity, Eq. (33) is reformed as

$$ln\, j = \int_\Gamma \frac{m\phi_0^m exp(mL)dL}{(1-\phi_0^m exp(mL))}, \quad (36)$$

where Γ is the 1-D domain as shown in Fig. 4a. Transforming the integrated part in right hand side term of Eq. (36) gives

$$f(Z) = \frac{m\phi_0^m exp(mL)}{(1-\phi_0^m exp(mL))} = \frac{m}{(\phi_0^{-m} exp(-mL) - 1)} = -m\frac{1}{(1-Z)}, \quad (37)$$

where $Z = \phi_0{}^{-m} exp(-mL)$. The Laurent series expansion of Eq. (37) is obtained as

$$ln\, j = \int_\Gamma \frac{m\phi_0{}^m exp(mL)dL}{(1-\phi_0{}^m exp(mL))} \quad (38)$$

$$= m\left(\frac{\phi_0^m exp(mL)}{m} + \frac{\phi_0^{2m} exp(2mL)}{2m} + \ldots\right) + C_6,$$

where C_6 is a constant determined by boundary conditions.

By selecting the number of terms adopted in the above derivations, the error can be reduced to an acceptable value. Taking only the first two terms as an example (and solving the left-hand-side of Eq. (38) for C by integration), the concentration distribution is

$$C \cong \int_\Gamma -\frac{\ell_0}{D} exp\left(\phi_0^m exp(mL) + \frac{\phi_0^{2m} exp(2mL)}{2} + C_6\right) dL. \quad (39)$$

Taking $G(L) = \phi_0^m exp(mL) + \frac{\phi_0^{2m} exp(2mL)}{2} + C_6$ and computing the Taylor series of the integrand of Eq. (39) with respect to $G(L)$ about zero, when only first two terms are selected, the integrating gives

$$C \cong -\frac{\ell_0}{D}\left(\left(1+\frac{C_6^2}{2}\right)L + \frac{(1+C_6)}{m}\phi_0^m exp(mL) + \frac{1}{2m}\phi_0^{2m}\left(1+\frac{C_6}{2}\right)exp(2mL) + \frac{1}{6m}\phi_0^{3m} exp(3mL) + \frac{1}{32m}\phi_0^{4m} exp(4mL) + C_7\right), \quad (40)$$

where C_6–C_7 are constants determined by boundary conditions. The solutions for $x >$ a follow the same procedure and the final expression can be found in Section A.3 of Appendix A.

For the same problem shown in Fig. 4a and $\phi_0 = 1.0$, solutions with n terms of the Laurent series and p terms of the Taylor series are shown in Fig. 5a-b. With the Taylor series term number fixed to 10, the Laurent series term number is increased to around 5000 to minimize the error. The solution is approximately a step function:

$$C = 0.0 \text{ for } x < a, \quad (41a)$$

$$C = 1.0 \text{ for } x > a. \quad (41b)$$

For the scenario with $\phi = 1.0$ at $x =$ a, the plate is completely fractured, and the diffusion pathway is blocked. The $x >$ a part forms a reservoir with a constant concentration with the value of left boundary. Similarly, $x >$ a part has no diffusion from the left side and all the concentration outflows from the right boundary. Fig. 5c-d shows the phase field distribution and concentration evolution for different ϕ_0 at, $x =$ a. The concentration is continuously distributed, and the change is limited until ϕ_0 reaches 1.0.

3.3. 1-D FEM solutions

To verify the accuracy of the numerical approach, a 1-D finite element model for the coupling of the diffusion field and phase field was implemented within MATLAB® and compared with the analytical results approximated with Laurent series expansion. The phase field parameter is preset and the concentration distribution is extracted from the modeling results to show the one way coupling of fracture to diffusivity. The process follows typical FEM modeling procedures: after initializing the concentration field, the Gauss integration locations and weights, shape function values (N matrix) and shape function derivative values (B matrix) are generated based on 2-node linear elements with 2 Gauss points. The meshing is then carried out by decomposing the whole domain into elements of identical lengths. The nodal, integration point and integration point phase field values are then stored into corresponding matrices, based on which the local K-matrix and RHS matrix for each element are generated. The global K-matrix and RHS matrix is then assembled and solved with the generalized minimum residual method solver within MATLAB® [43]. The corresponding pseudocode is included in Appendix B.

Three phase field parameter distributions were considered. The corresponding concentration distribution results fit well with the analytical results approximated with Laurent series expansion, as shown in Fig. 6. When ϕ_0 reaches 1.0, both the numerical and analytical results show the sudden change at the middle compliant point; the diffusion process is significantly reduced by this fully developed crack.

4. Corrosion-fracture process coupling verification

4.1. Volume change due to corrosion

As discussed in Section 2.1, a linear relation is assumed for the link between the volume expansion rate and the dissolved O_2 flux, as shown in Eq. (7). Volume expansion only occurs at the rust layer rather than within the concrete. Considering a uniform radial diffusion process where all dissolved O_2 are consumed by the corrosion process at the steel-concrete interface, for a circular case of a homogeneous material and a pre-crack as shown in Fig. 7a, the concentration boundary conditions are

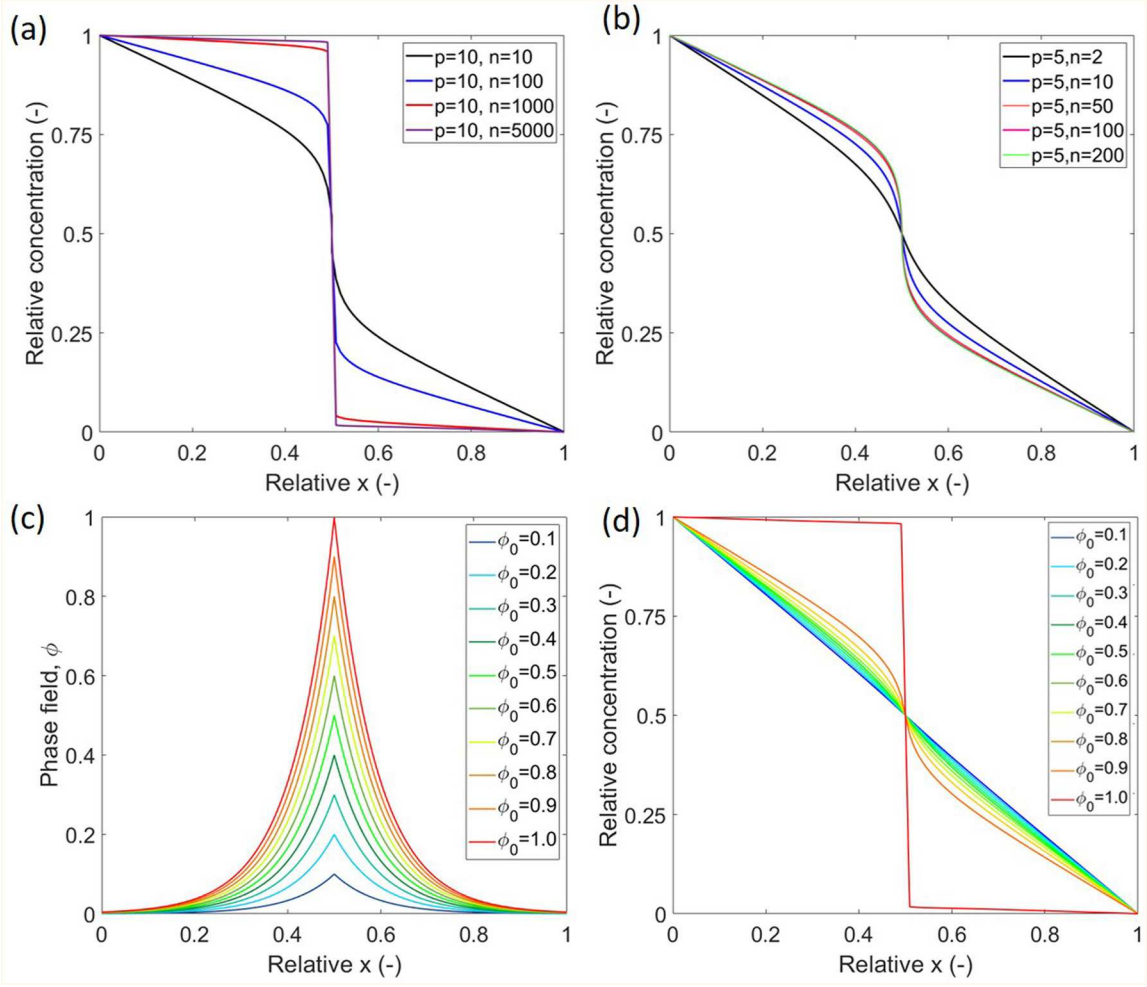

Fig. 5. (a–b) Laurent series solution with varying terms. (c–d) Laurent series solution for varying ϕ_0. Geometric variables and concentration values are normalized with the same method shown in Fig. 4.

$$C(r = r_1) = 0, C(r = r_2) = C_{r2}, \tag{42}$$

where r_1 and r_2 are the radius of the inside and outside boundary. Without the influence of the crack, the steady state diffusion will follow Fick's law of diffusion (where a constant diffusion coefficient is assumed in this case) in polar coordinates:

$$\nabla^2 C = \frac{1}{r}\frac{\partial}{\partial r}\left(r\frac{\partial C}{\partial r}\right) = 0. \tag{43}$$

The solution with applied boundary conditions is

$$C(r) = \frac{C_{r2}}{ln(r_2/r_1)} lnr - \frac{C_{r2} ln(r_1)}{ln(r_2/r_1)}. \tag{44}$$

The volume expansion will be uniformly developed along the hoop direction. Thus, the effects on the concrete cover is equivalent to a uniform displacement boundary condition on the interface in the radial direction.

Consider the gradient of concentration field at the interface, Γ_{int} (at $r = r_1$), is obtained as

$$\nabla C(r = r_1) = \frac{C_{r2}}{ln(r_2/r_1)}\frac{1}{r_1}. \tag{45}$$

The displacement of Γ_{int} in the radial direction is then calculated via the volumetric change of reinforcement,

$$R(t) = r_1\sqrt{1 + 2\pi\alpha t\frac{DC_{r2}}{ln(r_2/r_1)}}. \tag{46}$$

4.2. Linear elastic fracture mechanics (LEFM) analysis

To focus on the coupling of corrosion-fracture fields, the coupling of the diffusion-fracture fields is temporally suppressed by setting the diffusion coefficient, D, as a constant rather than correlated to the phase field parameter. In this setting, the boundary conditions given by Eq. (42) apply for all processes and the tensile hoop stress will create a mode-I scenario for the pre-crack as shown in Fig. 7b.

In LEFM, the crack initiation happens when the critical energy release rate, G_c, is reached, i.e., $G = G_c$. For a pre-crack with non-uniform mode-I loading conditions, the energy release rate, G, is found by taking $G = \frac{K_I^2}{E}$ where K_I is the mode-I stress intensity factor and is expressed in terms of a weight function based on a reference case. E is the Young's modulus. It was shown by Bueckner [44] that the weight function, h, should depend only on the geometry and not on the loading conditions (if defined as the form in following equation), thus the K_I under complex loading conditions could be calculated based on cases with identical geometries and simple loading conditions that have analytical solutions,

$$h(r) = \frac{E}{2K_I}\frac{\partial u}{\partial a} = \frac{E}{2K_{I,ref}}\frac{\partial u_{ref}}{\partial a}, \tag{47}$$

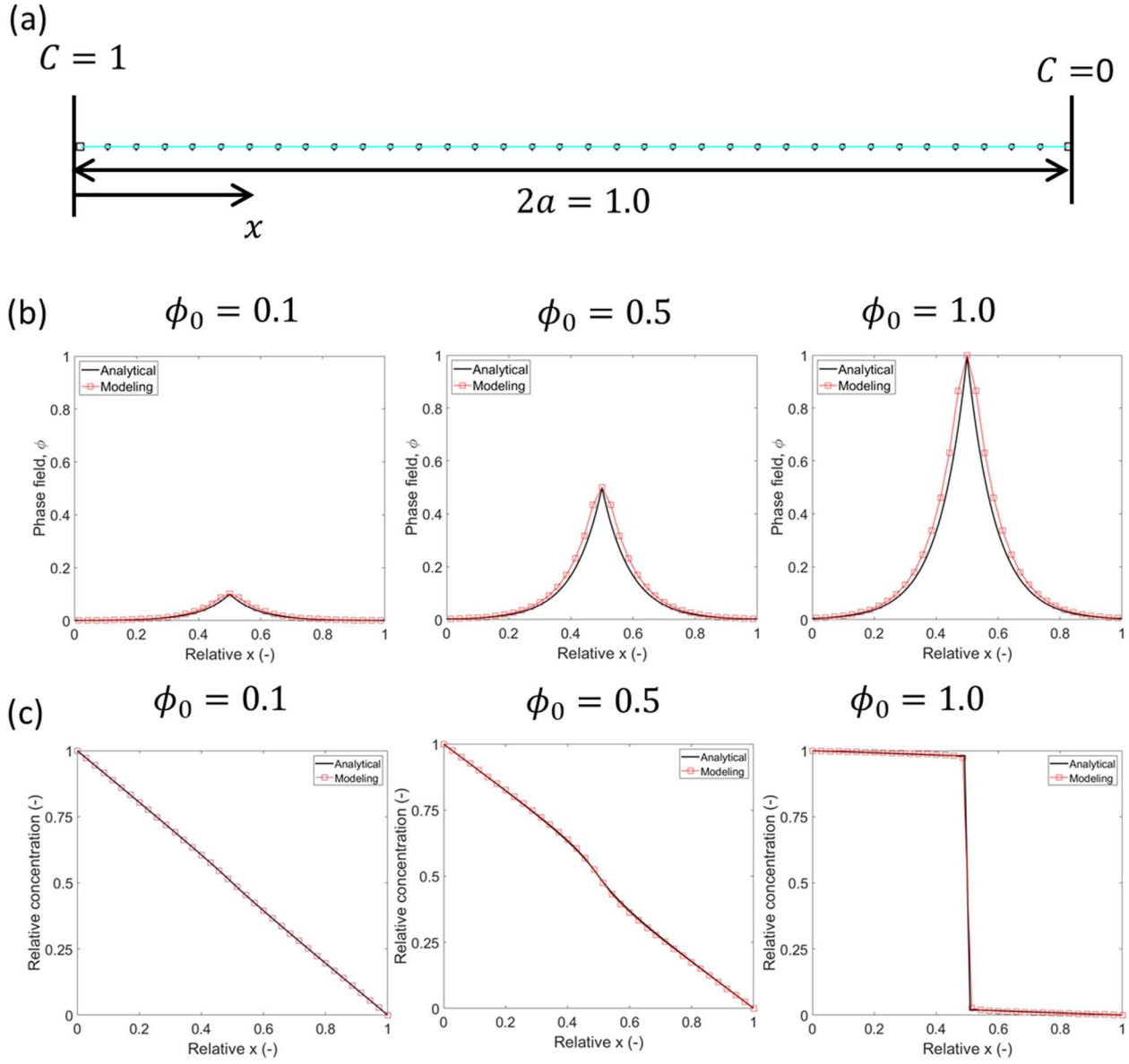

Fig. 6. (a) 1D FEM model setup. (b) Phase field and (c) concentration distribution for 1D FEM comparing with analytical solutions approximated with Laurent series. Geometric variables are normalized by the domain length as shown in (a), concentration values are normalized by the left end concentration.

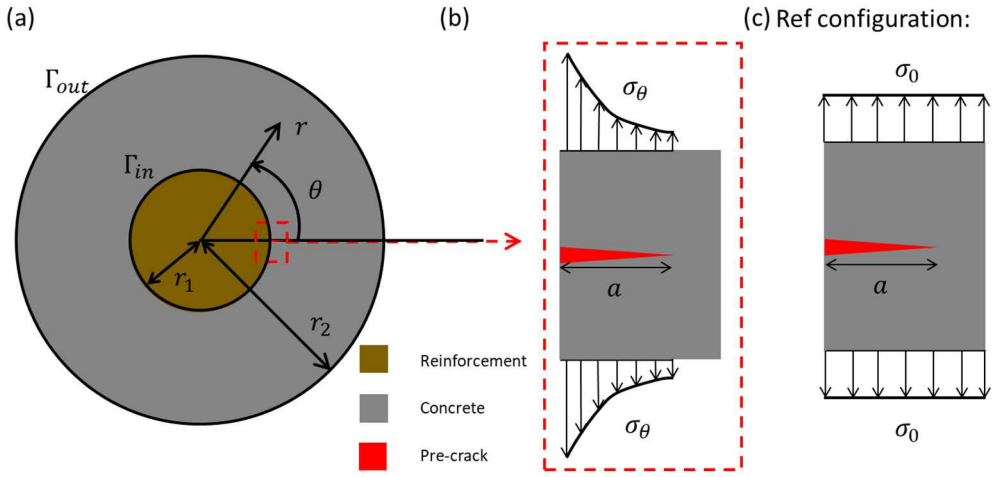

Fig. 7. (a) Analytical model for crack initiation. (b) Hoop stress distribution. (c) Reference configuration for weight function.

where a is the pre-crack length, E is the Young's modulus. K_I and u are the mode-I stress intensity and y-direction displacement field for the problem to be solved while $K_{I,\,ref}$ and u_{ref} are for the reference system. For a pre-crack with loading conditions shown in Fig. 7b, the weight function is obtained by using a reference case with identical geometry and known analytical stress intensity factor, i.e., a mode-I edge crack applied with a uniform loading. The pre-crack here is assumed to be a minor crack with crack length $a << r_1$. The stress intensity factor is then given by

$$K_I = \int_{\Gamma_c} p(r)h(r)dr, \tag{48}$$

where $p(r)$ is the loading and Γ_c is the pre-crack length.

Using Eq. (42) as the boundary conditions for the concrete cover shown in Fig. 7a, Lame's equation under plane strain conditions under a polar coordinate system is

$$\frac{d^2u_r}{dr^2} + \frac{1}{r}\frac{du_r}{dr} - \frac{1}{r^2}u_r = 0, \tag{49}$$

where the displacement, strain and stress fields are given by

$$u_r = \frac{A}{r} + Br,\ u_\theta = 0, \tag{50a}$$

$$\varepsilon_r = \frac{\partial u_r}{\partial r} = -\frac{A}{r^2} + B,\ \varepsilon_\theta = \frac{A}{r^2} + B, \tag{50b}$$

$$\sigma_r = \frac{E}{(1-2\nu)(1+\nu)}\left(-(1-2\nu)\frac{A}{r^2} + B\right), \sigma_\theta = \frac{E}{(1-2\nu)(1+\nu)}\left((1-2\nu)\frac{A}{r^2} + B\right), \tag{50c}$$

where A and B are constants depending on the boundary conditions and are given by

$$A = \frac{(R-r_1)r_2^2 r_1}{(r_2^2 + (1-2\nu)r_1^2)}, B = \frac{(1-2\nu)(R-r_1)r_1}{(r_2^2 + (1-2\nu)r_1^2)}. \tag{51}$$

The stress intensity factor for the reference case shown in Fig. 7c is

$$K_{I,ref} = 1.12R_{aw}\sigma_0\sqrt{\pi a}, \tag{52}$$

where σ_0 is the applied uniform stress, approximated with σ_θ in this case, and R_{aw} is the shape coefficient obtained with following,

$$R_{aw}\left(\frac{a}{r_2 - r_1}\right) = sec\left(\frac{\pi a}{2(r_2 - r_1)}\right)^{\frac{1}{2}}\left(1 - 0.025\left(\frac{a}{r_2 - r_1}\right)^2 + 0.06\left(\frac{a}{r_2 - r_1}\right)^4\right) \tag{53a}$$

The crack opening displacement for the reference system is obtained from the displacement field of the crack tip area with $\theta = \pi$ [45],

$$u_{ref} = \frac{4(1-\nu^2)}{E}K_{I,ref}\sqrt{\frac{r'}{2\pi}} = \frac{4.48(1-\nu^2)\sigma_0}{E}\sqrt{\frac{a(a-(r-r_1))}{2}}, \tag{53a}$$

$$\frac{\partial u_{ref}}{\partial a} = \frac{2.24R_{aw}(1-\nu^2)\sigma_0}{\sqrt{2}E}\left(\sqrt{\frac{a}{(a-(r-r_1))}} + \sqrt{\frac{(a-(r-r_1))}{a}}\right), \tag{53b}$$

where r' is the distance between the crack tip and the point of interest. Plugging Eq. (53b) into Eq. (47) and the weight function is obtained as

$$h(r) = \frac{E}{2K_{I,ref}}\frac{\partial u_{ref}}{\partial a} = \frac{(1-\nu^2)}{\sqrt{2\pi a}}\left(\sqrt{\frac{a}{(a-(r-r_1))}} + \sqrt{\frac{(a-(r-r_1))}{a}}\right) \tag{54}$$

Thus the mode-I stress intensity factor for Fig. 7b is obtained by plugging Eq. (54) into Eq. (48)

$$K_I = \int_{r_1}^{r_1+a}\sigma_\theta(r)h(r)dr$$

$$= E\frac{(1-\nu)}{\sqrt{2\pi a}}\left(A\sqrt{a}\left(-\frac{1}{2(a+r_1)^{\frac{3}{2}}}ln\left(\frac{\sqrt{(a+r_1)}-\sqrt{a}}{\sqrt{a}+\sqrt{(a+r_1)}}\right) + \frac{\sqrt{a}}{(a+r_1)r_1}\right) + \frac{A}{\sqrt{a}}\left(\frac{\sqrt{a}}{r_1} + \frac{1}{2}\frac{1}{\sqrt{(a+r_1)}}ln\left(\frac{\sqrt{(a+r_1)}-\sqrt{a}}{\sqrt{a}+\sqrt{(a+r_1)}}\right)\right) + \frac{8Ba}{3(1-2\nu)}\right) \tag{55}$$

The energy release rate is then obtained with

$$G = \frac{(1-\nu^2)K_I^2}{E}. \tag{56}$$

The time when G reaches the critical energy release rate G_c is recorded as the crack initiation time, which will later be compared with the numerical results in the next section.

4.3. Numerical implementation

Parameter studies are conducted with finite element modeling and compared with analytical solutions. The influences of geometric settings and material properties on the fracture development are considered in this study: the pre-crack length is chosen as the geometric variable; for the material property, the volume expansion rate per mole of dissolved O_2, α, and diffusion coefficient D have similar effects on the corrosion introduced volume expansion, i.e., it is expected that the volume expansion rate will be increased with either increased α and constant D or constant α and increased D. Since they are all of the first order from Eq. (7), we use their products, αD, to represent the influence of the material property change on the fracture development. The results are shown in Fig. 8.

Quarter circular cases with geometry shown in Fig. 8a were used for the model. A circular steel bar with radius of 3 mm served as the reinforcement and the concrete cover also had a uniform thickness of 3 mm. The x-direction displacement of the top boundary and the y-direction displacement of bottom boundary were constrained. The outside boundary has no displacement constraints. It is assumed that this concrete structure is within an environment with constant dissolved O_2 and all O_2 at the reinforcement-concrete interface is consumed. Correspondingly, the concentration is assumed to be 1.0 at the outside surface, Γ_{out}, and 0.0 at the inside surface, Γ_{in}. A pre-crack with length $a = 0.1r_1$ is introduced at the steel-concrete interface along the bottom boundary. Corresponding to the LEFM analysis, the crack initiation time is taken as the time when the phase field parameter at the crack tip reaches 0.99. The phase field distribution at this point in time is shown in Fig. 8b. The trend of crack initiation time obtained from the numerical approaches described in Section 2 with varying pre-crack length and αD fits well with the trends in the LEFM analytical results. The error increases with increasing pre-crack length, which is due to the assumption of minor cracks in the LEFM analysis. For both the numerical and analytical results, the crack initiation time decreases with increasing pre-crack length and αD value, where α is the volume expansion rate per mole of O_2 and D is the diffusion coefficient. LEFM analysis yields accurate crack initiation times when the crack length is small and uniform hoop stress conditions are applied. However, when the crack length increases and the interface displacement is influenced by the changing diffusion processes, the LEFM model fails to describe the real phenomena while the numerical model can still accurately simulate complex displacement and concentration conditions.

5. Fully interacted modeling

Now that the diffusion-fracture and corrosion-fracture coupling have been separately verified, steel bar reinforced and H-pile steel combined

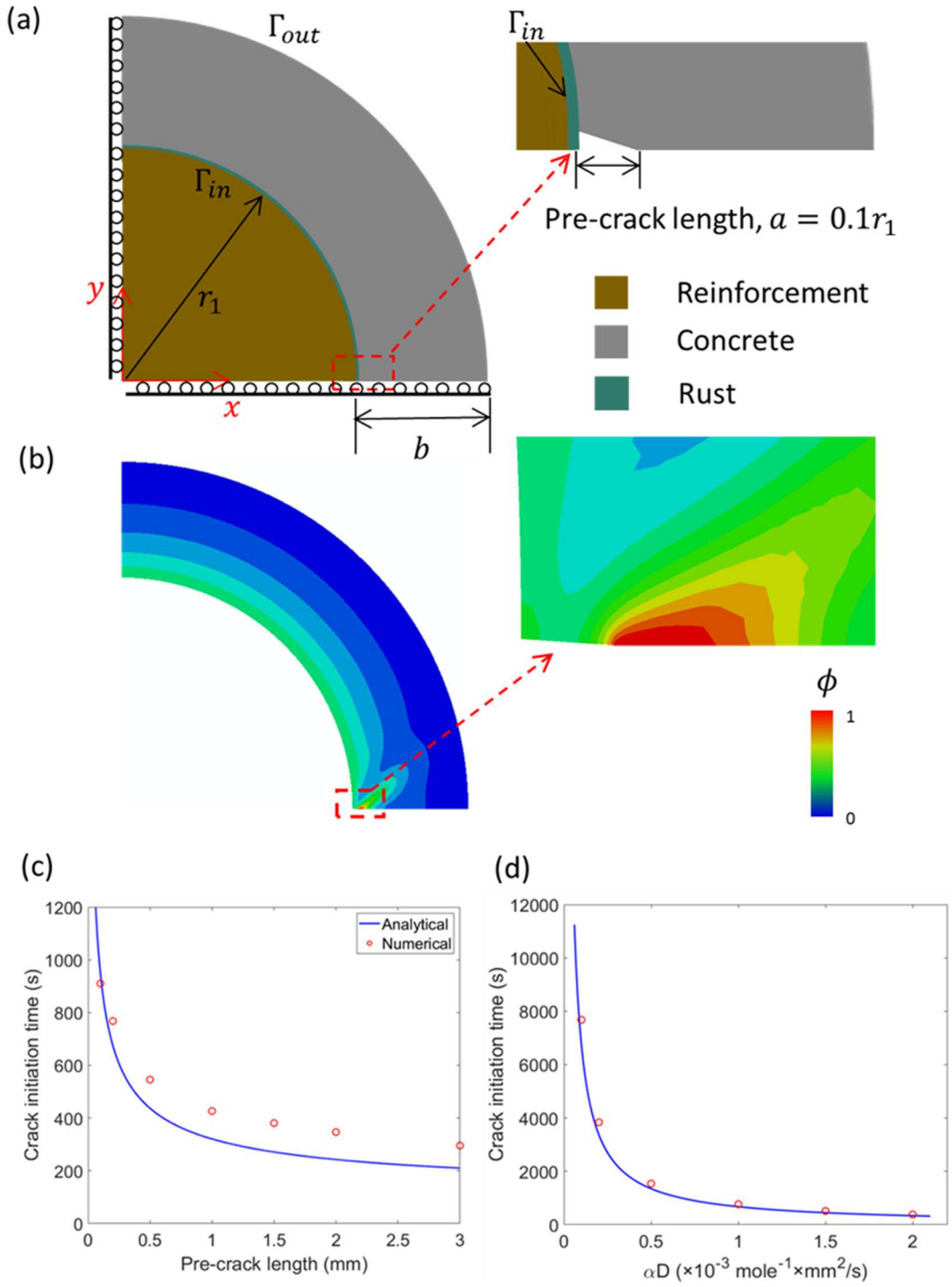

Fig. 8. (a) FEM model for crack initiation, where the inside boundary, Γ_{in} points to the interface of reinforcement and rust layer. (b) The phase field distribution of concrete at crack initiation step. (c-d) Crack initiation time step comparison with the analytical model.

concrete structures were modeled to study the corrosion induced fracture behavior based on the formulation and numerical implementation processes discussed in Section 2. For computational efficiency, quarter structures were simulated to take advantage of symmetry.

5.1. Cylindrical concrete cover

First, a series of quarter circular cases are simulated with geometry shown in Fig. 8a. The crack propagation and corresponding concentration distribution for different stages are shown in Fig. 9. With the crack propagating, a diffusion channel is generated and the flux of oxygen is directed into the channel. As shown in Fig. 9g, along the route Γ_θ shown in Fig. 9c and f, for a large θ where the phase field parameter remains at a low level, the concentration distribution is only slightly influenced. With θ becoming lower, the phase field parameter increases rapidly while approaching the crack and the concentration increases correspondingly after slightly decreasing, showing that crack propagation accelerates the diffusion process.

The crack propagation was characterized by relating the crack length to time steps for different variables as shown in Fig. 10. Three stages are

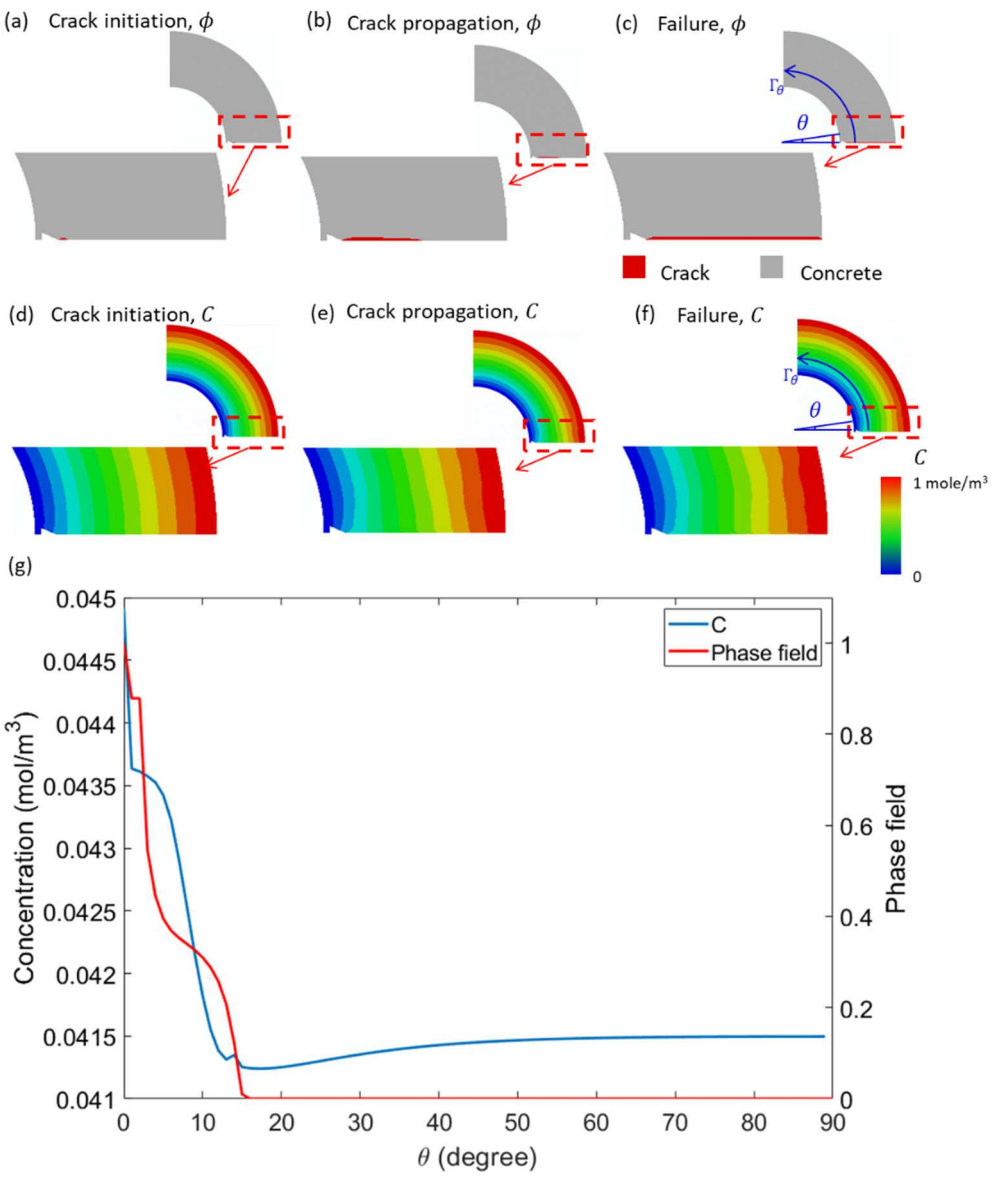

Fig. 9. (a–f) ϕ and C contour of concrete for critical time steps. (g) ϕ and C distribution along route Γ_θ as shown in (e) and (f).

found in this process. (1) The first stage begins at the start of the simulation until crack initiation. This stage includes the time steps required for the dissolved O_2 and Cl^- to reach the interface of the reinforcement and concrete and the energy release rate of the crack tip area reaching the critical value. (2) The second stage corresponds to the time steps required for the crack to propagate to the outer boundary. With the crack length increasing, the diffusion process is accelerated and thus rust accumulates faster, meanwhile, the system becomes more compliant and the time step needed for a unit increase in crack length decreases, resulting in a decreasing slope of the crack position versus time. (3) The third stage begins when the crack reaches the outer surface and the crack has reached its maximum length. At this point, the crack width will enlarge and concrete cover palling effects will be the main effects of this stage. Thus, the critical points in time correspond to crack initiation, t_1, and failure, t_2.

Following the same procedures, the influence of material properties on the crack propagation was also studied. For different G_c and αD, crack propagation also follows the 3-stage behavior but with different crack initiation and propagation time steps. The crack initiation and failure time steps were determined for varying G_c and αD as shown in Fig. 11. As αD increases, the corrosion process is promoted and more rust is accumulated and the crack initiation and propagation processes are accelerated. As a result, the critical times for crack initiation and failure decrease. As G_c increases, a higher stress field will be needed for crack initiation. Thus, the propagation processes are delayed.

5.2. *H-pile steel with concrete jacket*

H-pile steel is widely used in bridge and other transportation structures. After being exposed to aggressive environments, severe localized corrosion damage has been detected in these weight supporting components, which endangers the serviceability and durability. Many repair techniques could be used to restore the loading and buckling capacity to the design level. Compared to enhancement approaches on the flange with steel channels [46], the application of concrete jackets provides extra protection against the environmental erosion as well as alternative load paths to increase the loading capacity [47]. Like many other steel-concrete structures, the failure of fracture in concrete jackets due to H-pile steel expansion introduced by loading or corrosion are the main reasons for the serviceability loss. To understand this failure process, which is essential for the design of repair approaches for such types of structures, experimental studies have been conducted with push-out

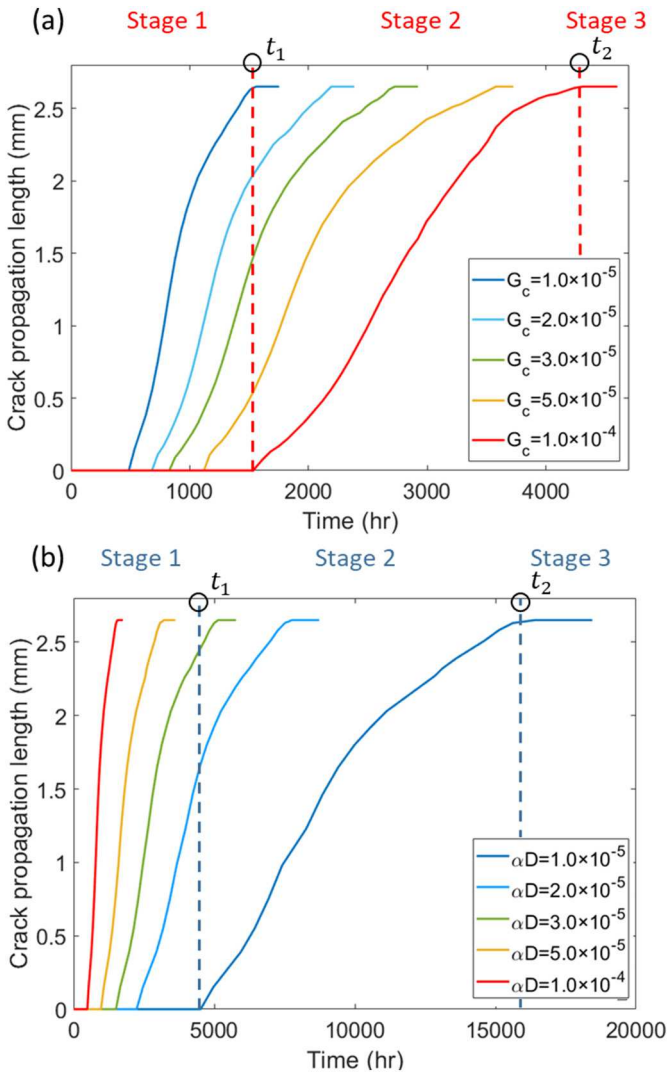

Fig. 10. Crack length (normalized with the reinforcement radius) with respect to time for varying (a) G_c (unit: J/mm^2) and (b) αD (unit: mole^{-1} × mm^2/s), where t_1 and t_2 are for critical time of crack initiation and failure.

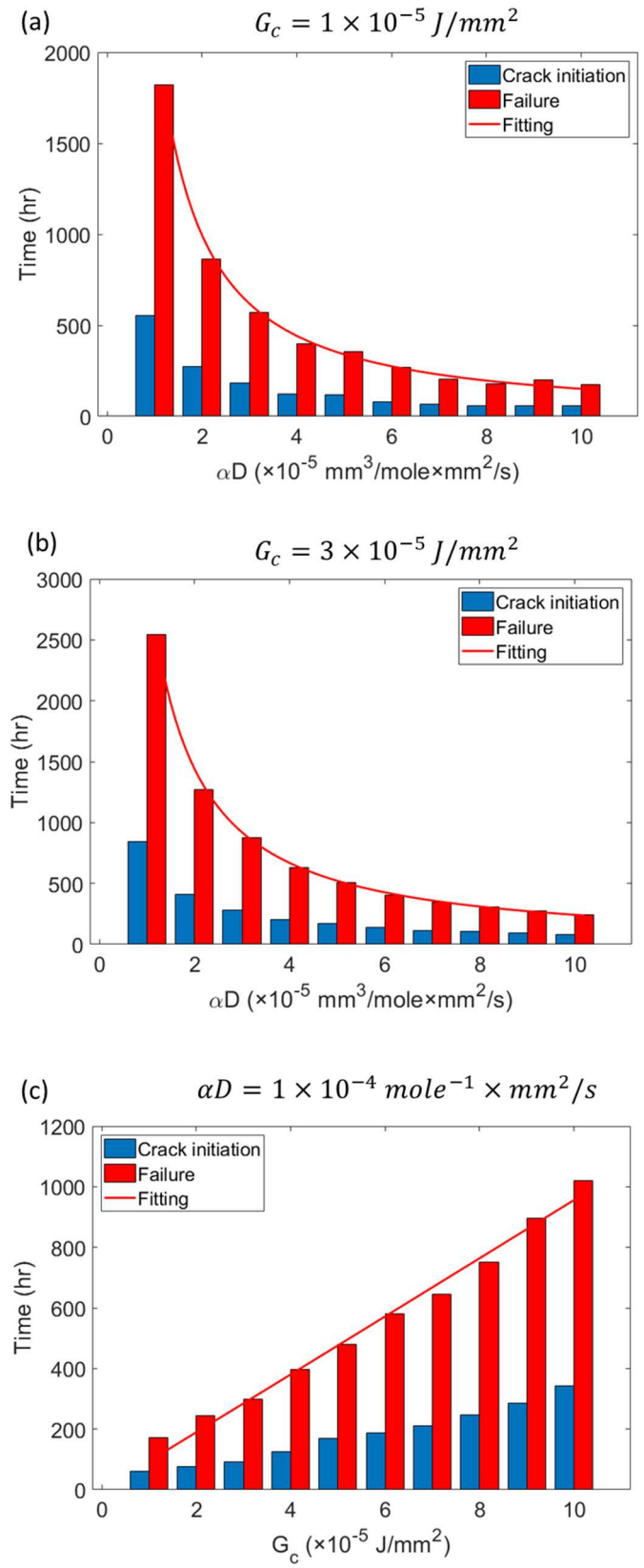

Fig. 11. Critical times for crack initiation and failure for different (a-b) αD and (c) G_c.

tests [48]. However, numerical or analytical analysis on the failure processes of loading or corrosion-introduced concrete jacket failure are still lacking.

In this section, the push-out induced concrete jacket fracture behavior was modeled with the proposed phase field formulation in two loading steps following the experiment in [49]. The mechanical loading was modeled first to calibrate the proposed phase-field model. The corrosion induced fracturing was modeled subsequently to understand the long-term reliability of the structure. In accordance with the experiments, a combined structure with HP250×62 H-pile steel and concrete jacket as shown in Fig. 12a with a radius of $r = 254$ mm was used in the numerical modeling. A quarter of the cross section as shown in Fig. 12b was used for computational efficiency, taking advantage of symmetry. As shown in Fig. 12b, at the top and bottom boundaries, the displacement components are constrained along the x- and y-direction, respectively. For push-out induced fracture, a z-direction loading scenario was considered. The equivalent boundary conditions are applied on the inside boundary, Γ_{in}, with following approach: for a given applied global strain, ε_z, the resulting in-plane displacement at the steel-concrete interface was calculated via Poisson's ratio of the steel and applied on Γ_{in}. Considering that the Young's modulus of steel could be 9–10 times higher than that of concrete, the steel is then assumed to be rigid

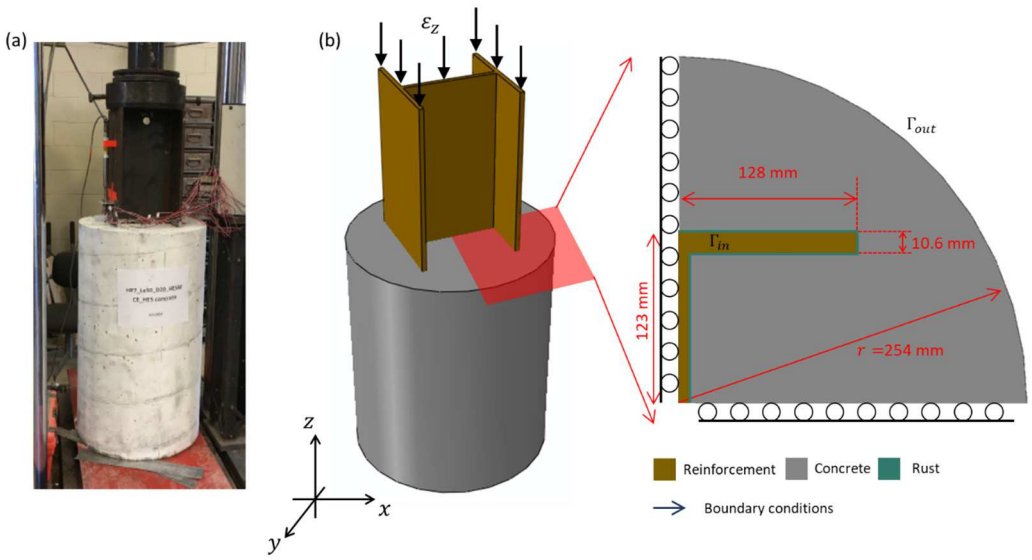

Fig. 12. (a) H-pile steel with concrete jackets under push-out experiments [49]. (b) Geometry of the quarter section structure used in the phase field model.

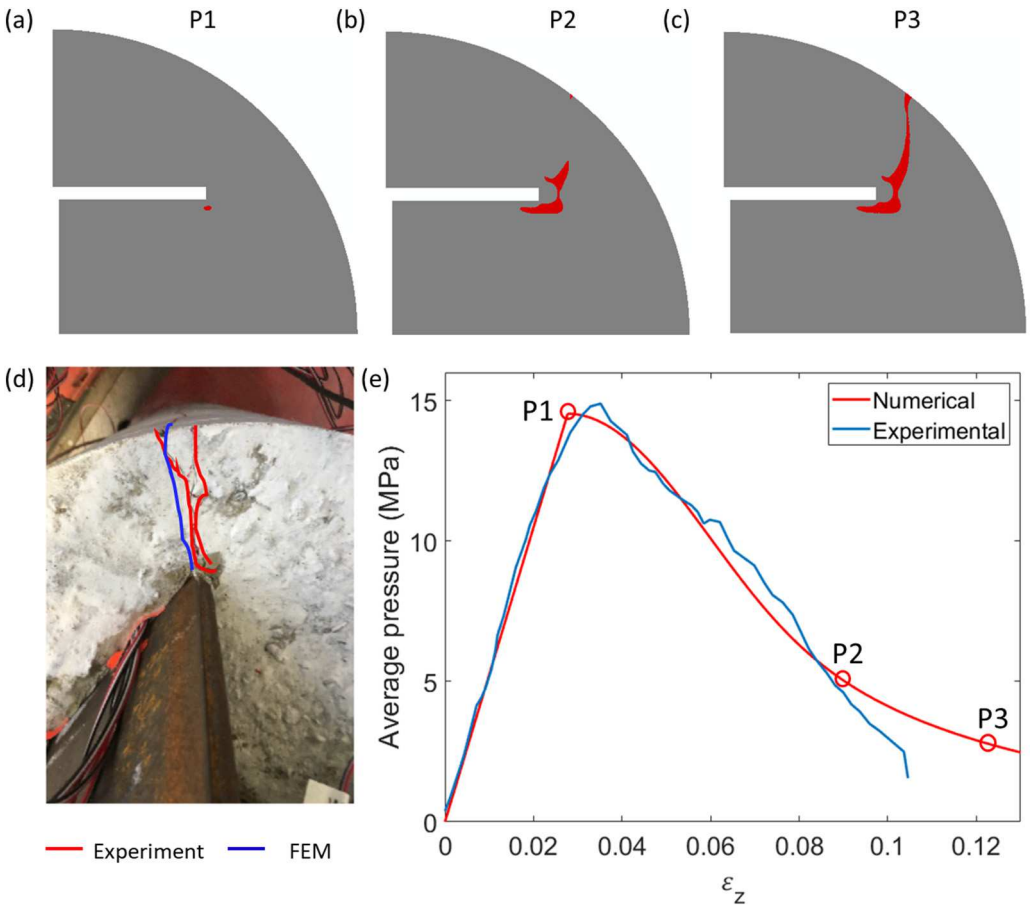

Fig. 13. (a–c) Crack propagation of critical steps under push-out modeling of concrete jackets with the phase field formulation. (d) Concrete jacket crack patterns in push-out experiments [49] and numerical modeling. (e) Average pressure on the inside boundary versus strain applied along the z-direction.

relatively to concrete, so that elastic mismatch between steel and concrete can be neglected. The outside boundary, shown as Γ_{out} in Fig. 12b, is free to move.

The critical steps of the crack propagation caused only by the mechanical loading are shown in Fig. 13a-c and show a similar pattern with the experimental results as shown in Fig. 13d. The propagation angles have some difference, which may come from the randomly distributed aggregates and micro-cracks in concrete. The average confining pressure on the steel-concrete interface is shown in Fig. 13e. The modeling result was found to be in close agreement with the experimental data. The crack initiates from the lower corner of the H-pile steel flange, which is due to the stress concentration induced by the geometry. The stress

concentration at the upper corner also leads to crack initiation and propagation before it connects to the crack initiated from the lower corner. Afterwards, the crack propagates towards Γ_{out} until final failure. Correspondingly, the average pressure increases linearly before crack initiation, and then starts to drop due to the material degradation induced by fracture development. The drop is sharp at first and then the slope decreases until the reaction force reaches nearly 0.0, indicating the final failure of the H-pile steel-concrete combined structure.

For corrosion induced fracture, the push-out loading is first applied until the average pressure on Γ_{in} reaches 70% of the maximum pressure (the peak pressure point P1 as shown in Fig. 13e) to model the stress introduced by the supported upper bridge parts. Corrosion is not considered during this pre-loading process. After the pre-loading, the diffusion field is then introduced by setting the concentration as 1.0 on Γ_{out} and 0.0 on Γ_{in} boundaries separately. The corrosion effects on the fracture behavior were modeled using the proposed phase field formulation. Fracture development and concentration distribution fields are shown in Fig. 14a-c and e-f, respectively. The average pressure after the diffusion field is introduced is calculated and shown in Fig. 14 g. The crack initiates from the H-pile steel flange corners as shown in Fig. 14a, and propagates as shown in Fig. 14b, before final failure shown in Fig. 14c. As a result of the crack propagation, a diffusion channel is formed that accelerates the dissolved O_2 flux, as shown in Fig. 14d-f. This accelerated diffusion further aggravates the corrosion which continues to promote crack propagation until the crack grows through the concrete cover. The average pressure first increases nonlinearly until reaching the maximum value corresponding to the crack initiation step shown in Fig. 14a. Afterwards, a sudden average pressure drop was observed. This pressure drop continues until it falls below the initial pressure value under the pre-load, indicating the H-pile starts losing load bearing capacity. This pressure degradation continues until the concrete cover is cracked through and the H-pile completely loses its load bearing capacity.

Using the model, the effect of concrete diffusivity (αD) on crack propagation was investigated. As shown in Fig. 14 h, increasing αD leads to the delayed crack initiation time. The peak average pressure, however, stays almost constant with varying αD. This indicates that the increased permeability will only affect the long-term durability of the H-pile, but it does not affect the peak strength. This brief case study demonstrates the capability of the proposed phase-field formulation to model structural scale, durability related problems.

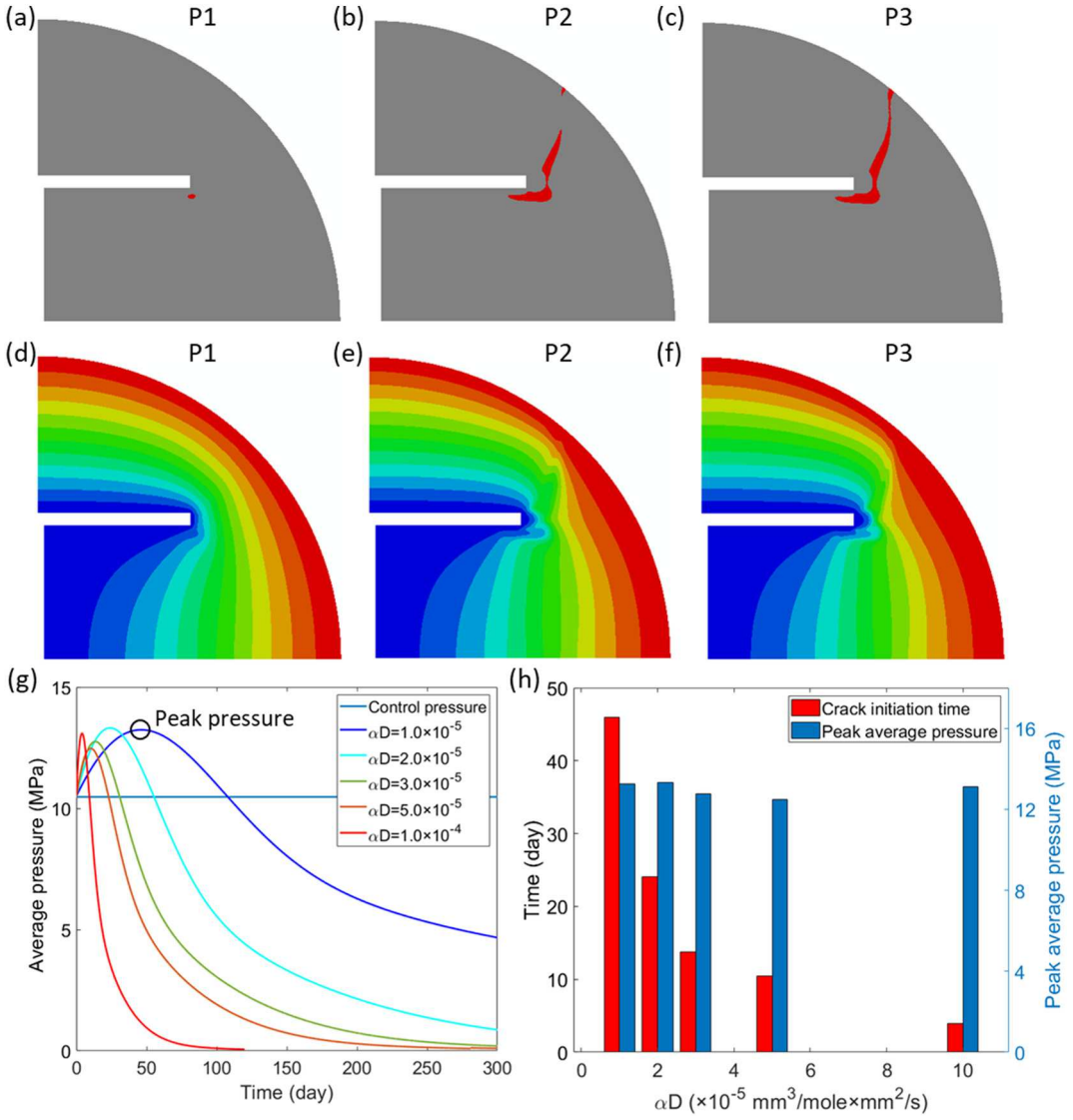

Fig. 14. (a–c) Corrosion induced crack propagation of critical times for concrete jackets. (d-f) Concentration distribution for critical steps. (g) Reaction force on the inside boundary with respect to time for varying αD (unit: mole^{-1} × mm^2/s). (h) Crack initiation time and peak average pressure with respect to varying αD.

6. Conclusions

A hydro-chemo-mechanical phase field formulation for corrosion induced fracture problems was constructed and verified. The FEM solutions to three corrosion induced cracking problems ranging from the steel-concrete interface scale to the structural scale were calculated. These solutions demonstrated the feasibility of applying the proposed formulation to a wide range of corrosion induced durability problems of concrete structures. The specific conclusions are summarized below.

(1) *Simultaneous solutions to multifield coupling*

The proposed formulation can successfully model the cracking induced change in the diffusion field, as well as the associated changes in corrosion reactions at the steel-concrete interface. This, for the first time, directly linked the diffusion to rust, and eventually to fracture and mechanical strains.

(2) *Failure prediction at both the interface scale and structural scale*

The proposed formulation demonstrates the feasibility of modeling damage in terms cracking and straining with corrosion at the interface scale. This enables the investigation of corrosion induced deterioration of steel-concrete interface as well as concrete cover spalling associated with corrosion induced cracking. In addition, the H-pile modeling results demonstrate a successful structural response prediction while maintaining a highly coupled simulation using the proposed formulation.

Author statement

The author Congjie Wei conducted the coding and computational work for the paper, Chenglin Wu provided funding support and designed the theoretical framework, Charles Wojnar provided technical supervision, especially on the numerical implementation. All authors participated in the manuscript preparation effort.

Declaration of competing interest

The authors claim no conflict of interests.

Acknowledgement

This material is based upon work supported by the National Science Foundation under Grant No. MoMS 1930881. Financial support from the Material Research Center at the Missouri University of Science and Technology is also appreciated.

Appendix A. Derivation for diffusion field evolution with known fracture field

This appendix presents the derivation details for Sections 3.1–3.2.

A.1. 1D general form

Starting from Eq. (14):

$$\frac{dC}{dt} = \nabla\cdot(\boldsymbol{D}\nabla C) = \nabla\cdot((D(1-\phi^m)\boldsymbol{I} + \phi^m D(\boldsymbol{I} - \boldsymbol{n_1}\otimes\boldsymbol{n_1}))\nabla C) \text{ in } \Omega. \tag{A.1}$$

For 2-D steady flow state: $\frac{dC}{dt} = 0$ and

$$\boldsymbol{n_1} = \frac{\nabla\phi}{||\nabla\phi||} = \frac{1}{||\nabla\phi||}\begin{bmatrix}\frac{\partial\phi}{\partial x}\\ \frac{\partial\phi}{\partial y}\end{bmatrix}, \tag{A.2}$$

where $||\nabla\phi|| = \left(\left(\frac{\partial\phi}{\partial x}\right)^2 + \left(\frac{\partial\phi}{\partial y}\right)^2\right)^{\frac{1}{2}}$. Consider a scenario where the phase field ϕ varies only in the x-direction, or $\frac{\partial\phi}{\partial y} = 0$, then

$$\boldsymbol{n_1} = \begin{bmatrix}1\\0\end{bmatrix} \tag{A.3}$$

The diffusive coefficient $\boldsymbol{D}$ in Eq. (A.1) could then be obtained as

$$\boldsymbol{D} = (D(1-\phi^m)\boldsymbol{I} + \phi^m D(\boldsymbol{I} - \boldsymbol{n_1}\otimes\boldsymbol{n_1})) = \begin{bmatrix}D(1-\phi^m) & 0\\ 0 & D(1-\phi^m)\end{bmatrix} + \phi^m D\left(\begin{bmatrix}1 & 0\\ 0 & 1\end{bmatrix} - \begin{bmatrix}1 & 0\\ 0 & 0\end{bmatrix}\right) \tag{A.4}$$

$$= \begin{bmatrix}D(1-\phi^m) & 0\\ 0 & D(1-\phi^m)\end{bmatrix} + \phi^m D\begin{bmatrix}0 & 0\\ 0 & 1\end{bmatrix}$$

$$= \begin{bmatrix}D(1-\phi^m) & 0\\ 0 & D\end{bmatrix} \tag{A.5}$$

Plug Eq. A.5 into Eq. (A.1) and consider 2-D steady flow state, i.e., $\frac{dC}{dt} = 0$,

$$0 = \nabla\cdot(D(1-\phi^m)\boldsymbol{I} + \phi^m D\,(\boldsymbol{I} - \boldsymbol{n_1}\otimes\boldsymbol{n_1})\,)\nabla C = \nabla\cdot\left(\begin{bmatrix} D(1-\phi^m) & 0 \\ 0 & D \end{bmatrix}\begin{bmatrix} \frac{\partial C}{\partial x} \\ \frac{\partial C}{\partial y} \end{bmatrix}\right) \tag{A.6}$$

$$= \nabla\cdot\left(\begin{bmatrix} D(1-\phi^m)\frac{\partial C}{\partial x} \\ D\frac{\partial C}{\partial y} \end{bmatrix}\right)$$

$$= \frac{\partial}{\partial x}\left(D(1-\phi^m)\frac{\partial C}{\partial x}\right) + \frac{\partial}{\partial y}\left(D\frac{\partial C}{\partial y}\right)$$

$$= -mD\phi^{m-1}\frac{\partial\phi}{\partial x}\frac{\partial C}{\partial x} + D(1-\phi^m)\frac{\partial^2 C}{\partial x^2} + D\frac{\partial^2 C}{\partial y^2}.$$

Adopting the assumption $\frac{\partial\phi}{\partial y} = 0$, then the concentration also remains constant along the y-direction. Eq. (A.6) is rewritten as

$$m\phi^{m-1}\frac{\partial\phi}{\partial x}\frac{\partial C}{\partial x} = (1-\phi^m)\frac{\partial^2 C}{\partial x^2}. \tag{A.7}$$

Rewriting Eq. (28) here,

$$\phi(x) = \phi_0 exp\left(-\frac{|x-a|}{\ell_0}\right) \tag{A.8}$$

For $x < a$, Eq. (A.8) turns to

$$\phi(x) = \phi_0 exp\left(\frac{x-a}{\ell_0}\right) \tag{A.9}$$

The gradient of ϕ along x-axis is then,

$$\frac{\partial\phi}{\partial x} = \frac{\partial}{\partial x}\left(\phi_0 exp\left(\frac{x-a}{\ell_0}\right)\right) = \frac{\phi_0}{\ell_0} exp\left(\frac{x-a}{\ell_0}\right) \tag{A.10}$$

Eq. (A.7) is then rewritten as

$$\frac{\partial^2 C}{\partial x^2} - \frac{m\phi_0^m exp\left(\frac{m(x-a)}{\ell_0}\right)}{\ell_0\left(1-\phi_0^m exp\left(\frac{m(x-a)}{\ell_0}\right)\right)}\frac{\partial C}{\partial x} = 0. \tag{A.11}$$

Taking $j = -D\frac{dC}{dx}$ as the flux, where D is the diffusion coefficient, taking $L = \frac{(x-a)}{\ell_0}$ for simplicity, thus $dL = \frac{1}{\ell_0}dx$, and substituting into Eq. (A.11) yields

$$\frac{\partial j}{\partial x} = \frac{m\phi_0^m exp(mL)}{\ell_0(1-\phi_0^m exp(mL))}j. \tag{A.12}$$

Following Eq. (A.12) and taking $\frac{\partial j}{\partial x} = \frac{dj}{dx}$, using the fact that $dx = \ell_0 dL$, Eq. (A.12) is then

$$\frac{dj}{j} = \frac{m\phi_0^m exp(mL)}{\ell_0(1-\phi_0^m exp(mL))}dx = \frac{m\phi_0^m exp(mL)dL}{(1-\phi_0^m exp(mL))}. \tag{A.13}$$

Integration of Eq. (A.13) along the 1D domain Γ leads to

$$\int_\Gamma \frac{dj}{j} = lnj = \int_\Omega \frac{m\phi_0^m exp(mL)dL}{(1-\phi_0^m exp(mL))}. \tag{A.14}$$

A.2. Analytical solution

For $x < a$, the following inequalities apply: $L = \frac{(x-a)}{\ell_0} < 0$, $0 < \exp(mL) < 1$, and $(1 - \exp(mL)) > 0$.
For scenarios with positive directed flux, i.e. $j > 0$, Eq. (A.14) leads to

$$lnj = \int_{\Gamma} \frac{m\phi_0^m exp(mL)dL}{(1-\phi_0^m exp(mL))} = \int_{\Gamma} \frac{m\phi_0^m dL}{(exp(-mL)-\phi_0^m)}$$

$$= -mL - ln\left(exp(-mL)-\phi_0^m\right) + C_1, \tag{A.15}$$

where C_1 is a constant. Exponentiating both sides yields

$$exp(lnj) = exp\left(-mL - ln\left(exp(-mL)-\phi_0^m\right) + C_1\right)$$

$$exp(lnj) = j = -D\frac{dC}{dx} = \frac{C_2 exp(-mL)}{exp(-mL)-\phi_0^m}, \tag{A.16}$$

where $C_2 = \exp(C_1)$. Integrating Eq. (A.16) leads to

$$C = \frac{C_2\ell_0}{D}\left(-L + \frac{1}{m}ln\left(\phi_0^{-m} - exp(mL)\right)\right) + C_3 = \frac{C_2\ell_0}{D}\left(-\frac{(x-a)}{\ell_0} + \frac{1}{m}ln\left(\phi_0^{-m} - exp\left(\frac{m(x-a)}{\ell_0}\right)\right)\right) + C_3. \tag{A.17}$$

Following same procedures, for $x > a$

$$C = \frac{C_4\ell_0}{D}\left(-L - \frac{1}{m}ln\left(\phi_0^{-m} - exp(-mL)\right)\right) + C_5 = \frac{C_4\ell_0}{D}\left(-\frac{(x-a)}{\ell_0} - \frac{1}{m}ln\left(\phi_0^{-m} - exp\left(-\frac{m(x-a)}{\ell_0}\right)\right)\right) + C_5, \tag{A.18}$$

where C_2–C_5 are constants.

A.3. Approximation of singularity with Laurent expansion

For $x < a$, take $Z = \phi_0^{-m}\exp(-mL)$ and the rewritten integrand term of Eq. (A.14) as

$$f(Z) = \frac{m\phi_0^m exp(mL)}{(1-\phi_0^m exp(mL))} = -\frac{m}{(1-\phi_0^{-m}exp(-mL))} = -\frac{m}{(1-Z)}. \tag{A.19}$$

For Eq. (A.19), the following conditions hold

$$L = \frac{x-a}{\ell_0} < 0, Z = \phi_0^{-m}exp(-mL) > 1. \tag{A.20}$$

For any analytic function $g(Z)$ on the annulus: $r_1 < |Z - Z_0| < r_2$, its Laurent series expansion is expressed as,

$$g(Z) = \sum_{n=1}^{\infty} \frac{b_n}{(Z-Z_0)^n} + \sum_{n=0}^{\infty} a_n (Z-Z_0)^n, \tag{A.21}$$

where

$$a_n = \frac{1}{2\pi i}\int_{\gamma} \frac{g(\omega)}{(\omega - Z_0)^{n+1}} d\omega, \tag{A.22}$$

$$b_n = \frac{1}{2\pi i}\int_{\gamma} g(\omega)(\omega - Z_0)^{n-1} d\omega, \tag{A.23}$$

and where γ is any circle $|\omega - Z_0| = r$ inside the annulus. Specializing for our case,

$$\frac{1}{1-Z} = \left\{ \begin{array}{l} \sum_{n=0}^{\infty} Z^n, |Z| < 1 \\ -\sum_{n=1}^{\infty} \frac{1}{Z^n}, |Z| > 1 \end{array} \right\} \tag{A.24}$$

Plug Eq. (A.24) into Eq. (A.19)

$$f(Z) = -m\frac{1}{(1-Z)} = m\sum_{n=1}^{\infty}\frac{1}{Z^n}$$

$$= m\left(\phi_0^m exp(mL) + \phi_0^{2m} exp(2mL) + \ldots\right) \tag{A.25}$$

Plugging Eq. (A.25) into Eq. (A.14) and yields

$$lnj = \int_{\Gamma} \frac{m\phi_0^m exp(mL)dL}{(1-\phi_0^m exp(mL))}$$

$$= m\left(\frac{\phi_0^m exp(mL)}{m} + \frac{\phi_0^{2m} exp(2mL)}{2m} + \ldots\right) + C_6. \tag{A.26}$$

Taking the first two terms:

$$lnj \cong \phi_0^m exp(mL) + \frac{\phi_0^{2m} exp(2mL)}{2} + C_6. \tag{A.27}$$

Exponentiating both sides, then integrating yields

$$\int_{\Gamma} dC = C = \int_{\Gamma} -\frac{\ell_0}{D} exp\left(\phi_0^m exp(mL) + \frac{\phi_0^{2m} exp(2mL)}{2} + C_6\right) dL. \tag{A.28}$$

In order to integrate the above expression we consider function $G(L) = \phi_0^m exp(mL) + \frac{\phi_0^{2m} exp(2mL)}{2} + C_6$ and compute the Taylor series of the integrand with respect to $G(L)$. Eq. A.28 is then expanded as

$$C = \int_{\Gamma} -\frac{\ell_0}{D} exp(\ G(L)\ ) dL = \int_{\Gamma} -\frac{\ell_0}{D}\left(1 + G(L) + \frac{1}{2!}\ G(L)^2 + \ldots\right) dL. \tag{A.29}$$

Just taking the first two terms, plugging $G(L)$ into (A.29), and integrating gives

$$C \cong -\frac{\ell_0}{D}\left(\left(1 + \frac{C_6^2}{2}\right)L + \frac{(1+C_6)}{m}\phi_0^m exp(mL) + \frac{1}{2m}\phi_0^{2m}\left(1 + \frac{C_6}{2}\right) exp(2mL) + \frac{1}{6m}\phi_0^{3m} exp(3mL) + \frac{1}{32m}\phi_0^{4m} exp(4mL) + C_7\right), \tag{A.30}$$

where C_6 and C_7 are integration constants. For $x > a$, following same procedure the concentration distribution is calculated as

$$C \cong -\frac{\ell_0}{D}\left(\left(1 + \frac{C_8^2}{2}\right)L - \frac{(1+C_8)}{m}\phi_0^m exp(-mL) - \frac{1}{2m}\phi_0^{2m}\left(1 + \frac{C_8}{2}\right) exp(-2mL) - \frac{1}{6m}\phi_0^{3m} exp(-3mL) - \frac{1}{32m}\phi_0^{4m} exp(-4mL)\right) + C_9, \tag{A.31}$$

where C_7–C_9 are constants.

Appendix B. Pseudocode for 1D FEM solution

The following pseudocode is for the 1D FEM solution of Section 3.3, where the lines starting with symbol '*' states the purpose of the following pseudocode.

* Input parameters: geometric settings, boundary conditions, number of nodes, constant variables and other necessary parameters.
* Initialized concentration field.
for each node.
concentration = zeros.
* Set Gauss integration locations and weights, N matrix and B matrix at integration point.
* Generate topology.
for each node.
topo = [location(1st node), location(2nd node)].
* Generate local K-matrix and RHS for each element.
for each element.
ϕ_{node}*=f(node location) with* Eq. (29)
$\phi_{int.\ point}$*=N*ϕ_{node}.
$\phi_{element}$*=* $\phi_{int.\ point}$
K_{local}*=*K_{local}*+0.5*D*(1-*$\phi_{element}^m$*)*B*B′*Int. weight*
RHS_{local}*=* RHS_{local}*+0.5*D*(1-*$\phi_{element}^m$*)*B*B′**$concentration_{node}$ ** Int. weight*
* Assemble global K-matrix and RHS
for each element
K_{global}*=*K_{global}*+*$K_{local\rightarrow global}$
RHS_{global}*=* RHS_{global}*+* $RHS_{local\rightarrow global}$
* Add boundary conditions to the U matrix

$U_{x=0} = 2$

$U_{x=L} = 0$

* Solve $K_{global}U = RHS$

References

[1] C. Lu, W. Jin, R. Liu, Reinforcement corrosion-induced cover cracking and its time prediction for reinforced concrete structures, Corros. Sci. 53 (4) (2011) 1337–1347.
[2] L. Chernin, D.V. Val, Prediction of corrosion-induced cover cracking in reinforced concrete structures, Constr. Build. Mater. 25 (4) (2011) 1854–1869.
[3] T. El Maaddawy, K. Soudki, A model for prediction of time from corrosion initiation to corrosion cracking, Cem. Concr. Compos. 29 (3) (2007) 168–175.
[4] L. Chernin, D.V. Val, K.Y. Volokh, Analytical modelling of concrete cover cracking caused by corrosion of reinforcement, Mater. Struct. 43 (4) (2010) 543–556.
[5] Y. Du, A. Chan, L. Clark, Finite element analysis of the effects of radial expansion of corroded reinforcement, Comput. Struct. 84 (13–14) (2006) 917–929.
[6] Y. Liu, Modeling the time-to corrosion cracking of the cover concrete in chloride contaminated reinforced concrete structures, PhD. diss, Virginia Tech., 1996.
[7] S.J. Pantazopoulou, K. Papoulia, Modeling cover-cracking due to reinforcement corrosion in RC structures, J. Eng. Mech. 127 (4) (2001) 342–351.
[8] L. Chun-Qing, R.E. Melchers, Z. Jian-Jun, Analytical model for corrosion-induced crack width in reinforced concrete structures, ACI Mater. J. 103 (4) (2006) 479.
[9] R.R. Hussain, T. Ishida, Enhanced electro-chemical corrosion model for reinforced concrete under severe coupled action of chloride and temperature, Constr. Build. Mater. 25 (3) (2011) 1305–1315.
[10] X. Zhu, G. Zi, A 2D mechano-chemical model for the simulation of reinforcement corrosion and concrete damage, Constr. Build. Mater. 137 (2017) 330–344.
[11] B. Yu, L. Yang, M. Wu, B. Li, Practical model for predicting corrosion rate of steel reinforcement in concrete structures, Constr. Build. Mater. 54 (2014) 385–401.
[12] C. Cao, M.M. Cheung, B.Y. Chan, Modelling of interaction between corrosion-induced concrete cover crack and steel corrosion rate, Corros. Sci. 69 (2013) 97–109.
[13] G. Nossoni, R.S. Harichandran, Electrochemical-mechanistic model for concrete cover cracking due to corrosion initiated by chloride diffusion, J. Mater. Civ. Eng. 26 (6) (2014), 04014001.
[14] R.D. Campilho, M.D. Banea, A.M.G. Pinto, Lucas F.M. da Silva, A.M.P. De Jesus, Strength prediction of single-and double-lap joints by standard and extended finite element modelling, Int. J. Adhes. Adhes. 31 (5) (2011) 363–372.
[15] T. Mohammadnejad, A. Khoei, An extended finite element method for hydraulic fracture propagation in deformable porous media with the cohesive crack model, Finite Elem. Anal. Des. 73 (2013) 77–95.
[16] K.M. Liew, X. Zhao, A.J. Ferreira, A review of meshless methods for laminated and functionally graded plates and shells, Compos. Struct. 93 (8) (2011) 2031–2041.
[17] G.C. Hsiao, O. Steinbach, W. Wendland, Boundary element methods: foundation and error analysis, in: Encyclopedia of Computational Mechanics, Second edition, 2017, pp. 1–62.
[18] T. Gantumur, Adaptive boundary element methods with convergence rates, Numer. Math. 124 (3) (2013) 471–516.
[19] Y. Rashid, Ultimate strength analysis of prestressed concrete pressure vessels, Nucl. Eng. Des. 7 (4) (1968) 334–344.
[20] G.A. Francfort, J.-J. Marigo, Revisiting brittle fracture as an energy minimization problem, J. Mech. Phys. Solids 46 (8) (1998) 1319–1342.
[21] M.A. Msekh, J.M. Sargado, M. Jamshidian, P.M. Areias, T. Rabczuk, Abaqus implementation of phase-field model for brittle fracture, Comput. Mater. Sci. 96 (2015) 472–484.
[22] G. Liu, Q. Li, M.A. Msekh, Z. Zuo, Abaqus implementation of monolithic and staggered schemes for quasi-static and dynamic fracture phase-field model, Comput. Mater. Sci. 121 (2016) 35–47.
[23] M. Ambati, R. Kruse, L. De Lorenzis, A phase-field model for ductile fracture at finite strains and its experimental verification, Comput. Mech. 57 (1) (2016) 149–167.
[24] M.J. Borden, T.J.R. Hughes, C.M. Landis, A. Anvari, I.J. Lee, A phase-field formulation for fracture in ductile materials: finite deformation balance law derivation, plastic degradation, and stress triaxiality effects, Comput. Methods Appl. Mech. Eng. 312 (2016) 130–166.
[25] T.-T. Nguyen, D. Waldmann, T.Q. Bui, Computational chemo-thermo-mechanical coupling phase-field model for complex fracture induced by early-age shrinkage and hydration heat in cement-based materials, Comput. Methods Appl. Mech. Eng. 348 (2019) 1–28.
[26] P. Zuo, Y.-P. Zhao, A phase field model coupling lithium diffusion and stress evolution with crack propagation and application in lithium ion batteries, Phys. Chem. Chem. Phys. 17 (1) (2015) 287–297.
[27] E. Martínez-Pañeda, A. Golahmar, C.F. Niordson, A phase field formulation for hydrogen assisted cracking, Comput. Methods Appl. Mech. Eng. 342 (2018) 742–761.
[28] W. Mai, S. Soghrati, R.G. Buchheit, A phase field model for simulating the pitting corrosion, Corros. Sci. 110 (2016) 157–166.
[29] W. Mai, S. Soghrati, New phase field model for simulating galvanic and pitting corrosion processes, Electrochim. Acta 260 (2018) 290–304.
[30] T. Wu, L. De Lorenzis, A phase-field approach to fracture coupled with diffusion, Comput. Methods Appl. Mech. Eng. 312 (2016) 196–223.
[31] M. Stefanoni, U. Angst, B. Elsener, Corrosion rate of carbon steel in carbonated concrete–a critical review, Cem. Concr. Res. 103 (2018) 35–48.
[32] R.R. Hussain, Effect of moisture variation on oxygen consumption rate of corroding steel in chloride contaminated concrete, Cem. Concr. Compos. 33 (1) (2011) 154–161.
[33] R.R. Hussain, T. Ishida, M. Wasim, Oxygen transport and corrosion of steel in concrete under varying concrete cover, w/c, and moisture, ACI Mater. J. (2012) 109(1).
[34] Y. Zhao, J. Yu, Y. Wu, W. Jin, Critical thickness of rust layer at inner and out surface cracking of concrete cover in reinforced concrete structures, Corros. Sci. 59 (2012) 316–323.
[35] C. Cao, M.M. Cheung, Non-uniform rust expansion for chloride-induced pitting corrosion in RC structures, Constr. Build. Mater. 51 (2014) 75–81.
[36] Y. Zhao, J. Dong, Y. Wu, W. Jin, Corrosion-induced concrete cracking model considering corrosion product-filled paste at the concrete/steel interface, Constr. Build. Mater. 116 (2016) 273–280.
[37] A. Akhavan, F. Rajabipour, Evaluating ion diffusivity of cracked cement paste using electrical impedance spectroscopy, Mater. Struct. 46 (5) (2013) 697–708.
[38] S.Y. Jang, B.S. Kim, B.H. Oh, Effect of crack width on chloride diffusion coefficients of concrete by steady-state migration tests, Cem. Concr. Res. 41 (1) (2011) 9–19.
[39] R.D. Cook, Concepts and Applications of Finite Element Analysis, John Wiley & Sons, 2007.
[40] C. Wei, C. Wu, C. Wojnar, Effect of patterned inclusions on the fracture behavior of ceramic composites, Compos. Part B 172 (2019) 564–592.
[41] D.L. Logan, A First Course in the Finite Element Method, Cengage Learning, 2011.
[42] C. Miehe, F. Welschinger, M. Hofacker, Thermodynamically consistent phase-field models of fracture: variational principles and multi-field FE implementations, Int. J. Numer. Methods Eng. 83 (10) (2010) 1273–1311.
[43] P.C. Hansen, Regularization tools version 4.0 for Matlab 7.3, Numer. Algorithms 46 (2) (2007) 189–194.
[44] H. Bueckner, Novel principle for the computation of stress intensity factors, Zeitschrift fuer Angewandte Mathematik & Mechanik **50** (9) (1970).
[45] T.L. Anderson, Fracture Mechanics: Fundamentals and Applications, CRC Press, 2017.
[46] B. Wan, Procedures, cost and effectiveness for deteriorated bridge substructure repair, in: Wisconsin Highway Research Program, 2013.
[47] K. Soliman, A. Arafa, T.M. Elrakib, Review of design codes of concrete encased steel short columns under axial compression, HBRC Journal 9 (2) (2013) 134–143.
[48] B. Grzeszykowski, E. Szmigiera, Ductility assessment of two-chord composite steel-concrete battened columns, Struct. Infrastruct. Eng. 13 (11) (2017) 1414–1424.
[49] M.M. Abdulazeez, A. Ramadan, B. Sherstha, A. Gheni, E. Gomaa, Y. Darwish, M. ElGawady, Behavior and Repair of Corroded Steel H-piles Phase I (Axial Behavior), Mid-America Transportation Center, 2019.